Institut für Neurowissenschaften
Technische Universität München

TLT

Mapping the functional micro-architecture of the primary auditory cortex with single-cell resolution in vivo

Carsten Tischbirek

Vollständiger Abdruck der von der Fakultät für Medizin der Technischen Universität München zur Erlangung des akademischen Grades eines

Doktors der Naturwissenschaften (Dr. rer. nat.)

genehmigten Dissertation.

Vorsitzender:

     Prof. Dr. Thomas Korn

Prüfende der Dissertation:

1. Prof. Dr. Arthur Konnerth
2. Prof. Dr. Michael Schemann
3. Prof. Dr. Olga Garaschuk

Die Dissertation wurde am 24.04.2018 bei der Technischen Universität München eingereicht und durch die Fakultät für Medizin am 07.11.2018 angenommen.

Abstract

The cortex is organized into functional regions corresponding, for example, to specific sensory modalities. Efforts to create maps of cortical functions involved various electrophysiological and/or imaging approaches. A major limitation in the interpretation of such maps has been the lack of knowledge of cell-specific activity patterns in deep cortical layers due to technical limitations. Here, we developed an improved two-photon Ca^{2+}-imaging approach based on the fluorescent Ca^{2+}-sensitive dye Cal-590 to record neuronal activity with single-cell resolution in all depths of the mouse cortex. We combined this technique with conventional two-photon imaging methods to build a map of the functional neuronal organization of all layers of the mouse primary auditory cortex. An accurate anatomical alignment of the individual imaged neurons with the global tonotopic gradient of the primary auditory cortex was achieved with large-scale autofluorescence imaging through the intact skull. Using this integrated procedure, we recorded spontaneous and tone-evoked activity of more than 1400 frequency-tuned neurons in all cortical layers. Pure-tone stimulation revealed that the averaged local response of neighboring neurons in all cortical depths had mostly similar but not identical tuning profiles, with a BF scatter of ~1 octave. Most strikingly, our results demonstrate that the tonotopy observed at the cortical surface is highly consistent with neuronal population responses recorded in all underlying cortical layers. Additionally, the spatial arrangement of local neuron populations responding to tone stimulation is characterized by smooth local BF gradients. Thus, the results provide the first functional map of all layers of a mammalian cortical region with single-cell resolution and reveal the micro-architecture of the primary auditory cortex.

Zusammenfassung

Die Großhirnrinde, auch Kortex genannt, ist in spezifische Areale eingeteilt, in der sensorische Modalitäten repräsentiert sind. Bemühungen, diese Regionen zu kartieren, beruhen auf einer Vielzahl von elektrophysiologischen und bildgebenden Verfahren. Eine große Einschränkung für die genaue Interpretation solch kortikaler Karten ist das Fehlen von Informationen über Nervenzell-spezifische Aktivität in den tiefen Schichten der Großhirnrinde. Im Rahmen dieser Arbeit wurde eine neue Methode entwickelt, um Nervenzellaktivität in allen Tiefen des Kortex der Maus zu untersuchen. Die Technik basiert auf Zwei-Photonenmikroskopie mit dem Kalzium-sensitiven Farbstoff Cal-590. In Kombination mit konventionellen Verfahren der Zwei-Photonenmikrokopie war es uns mit diesem Ansatz möglich, die neuronale Aktivität in allen Schichten des primären auditorischen Kortex zu untersuchen. Autofluoreszenz-Messungen durch den intakten Schädel erlaubten eine genaue Ausrichtung der zellulären Messungen am tonotopen Gradienten des primären auditorischen Kortex. Durch die Integration der verschiedenen Techniken konnte die spontane und Ton-induzierte Aktivität von 1400 Nervenzellen in allen Schichten des Kortex vermessen werden. Die Stimulation mit einzelnen Tonfrequenzen zeigte, dass die durchschnittliche lokale Antwort benachbarter Nervenzellen in allen kortikalen Tiefen ähnlich, aber nicht identisch ist und eine Streuung der besten-Frequenz-Antwort einzelner Nervenzellen von ungefähr einer Oktave hat. Erstaunlich war die Genauigkeit, mit welcher der tonotope Gradient, der an der Hirnoberfläche gemessen wurde, durch alle Schichten des Kortex hindurch auf der Ebene von Nervenzell-Gruppen erhalten blieb. Zusätzlich konnten wir beobachten, dass die räumlichen Antworten lokaler Gruppen von Nervenzellen auch auf sehr kurzen Entfernungen durch Frequenzgradienten charakterisiert sind. Zusammengefasst zeigt die Arbeit die erste funktionelle Karte aller Schichten einer kortikalen Region mit Einzelzell-Auflösung und beschreibt die Mikro-Architektur des primären auditorischen Kortex.

Acronyms

A1   Primary auditory cortex

AM   Acetoxymethyl-group

BF   Best frequency, which is the pure tone frequency evoking the largest neuronal response as measured with two-photon Ca^{2+} imaging

CA1   Cornu ammonis 1 area of the hippocampus

GCaMP   Genetically-encoded Ca^{2+} indicator protein, which contains circularly permutated green fluorescent protein, calmodulin and calmodulin-binding domain from the myosin light chain kinase

L2/3 to L6 Layer 2/3 to layer 6, which are the layers containing pyramidal neurons in the cortex

OGB-1   Oregon Green 488 BAPTA-1, name of fluorescent dye

ROI   Region of interest within an image used for data analysis

Contents

Contents

1. Introduction

1.1 Functional maps of the mammalian cortex

Cortical function is based on an intricate network of individual neurons organized according to strict structure-function relationships (Brodmann, 1909). An example for the connection between neuronal anatomy and network function is the representation of sensory modalities at specific areas of the cortex (Kalatsky *et al.*, 2005; Petersen, 2007; Wandell *et al.*, 2007). To gain a deeper understanding of the brain, functional maps of cortical areas were created using various electrophysiological and/or imaging techniques (Van Essen & Dierker, 2007; Glasser *et al.*, 2016). However, a major limitation in the interpretation of the areal maps has been the missing connection to cell-specific activity patterns of individual neurons, especially in deep cortical layers.

The mammalian cortex consists of up to six distinct cell layers (Brodmann, 1909). The most superficial layer, situated closest to the brain surface, is called layer 1. The deepest in turn is called layer 6. Electrophysiological measurements from the mid-20th century (Mountcastle *et al.*, 1955; Hubel & Wiesel, 1968) have shown that particular cortical areas are organized into vertical columns, which likely extend through the entire depth of the cortex from layer 1 to layer 6 and consist of neurons responsive to a specific sensory stimulation. The missing spatial resolution of the electrode recordings, however, occluded the exact spatial organization on the level of individual cells within such columns.

With the advent of two-photon microscopy, measurements of neuronal activity with single-cell resolution in intact brain tissue became possible. The technique allowed for the analysis of the functional organization of sensory-evoked neuronal activity in the upper layers of the cortex. For

example, in the primary visual cortex, one of the best-studied sensory cortical areas, direction-selective areas (responsive to visual stimuli moving into a specific direction) are arranged in a pinwheel-pattern in cats (Blasdel & Salama, 1986; Bonhoeffer & Grinvald, 1991). The cellular organization was revealed by two-photon imaging experiments (Ohki *et al.*, 2005), and two patterns for the organization of directions-selective neurons were described in cats: The first pattern are homogeneous patches of neurons selective to the same or very similar direction, and the second pattern are sharp edges between neighboring patches containing neurons selective to different directions. However, due to technical limitations (Peron *et al.*, 2015; Kondo *et al.*, 2016), the cellular organization in deeper cortical layers has not been analyzed, and a map of the functional neuronal microarchitecture for the representation of sensory-evoked activity extending through the entire depth of any cortical region currently does not exist. Thus, a link between the macroscale brain maps and cellular function in all layers of the cortex has not been described with single-cell resolution before.

1.2 Measuring Ca^{2+} transients in neurons

Two-photon Ca^{2+} imaging has become a well-established technique to study neuronal activity on a scale ranging from small, subcellular compartments such as dendritic spines (Chen *et al.*, 2011) to large-scale networks consisting of many thousand neurons (Stirman *et al.*, 2016). Besides its use for thick tissue slices, it is especially suitable for imaging experiments in the intact brain, for example during sensory stimulation or in combination with behavioral paradigms. Neuronal activity has been observed with single-cell resolution during behavioral experiments in, for example, drosophila (Seelig *et al.*, 2010), zebrafish (Brustein *et al.*, 2003), mouse (Komiyama *et al.*, 2010), rat (Sawinski *et al.*, 2009), and even non-human primates (Nauhaus *et al.*, 2012; Sadakane *et al.*, 2015).

The analysis of neuronal activity with two-photon microscopy is commonly based on the detection of changes of the intracellular Ca^{2+} concentration

with Ca^{2+}-sensitive fluorescent indicators (Grienberger & Konnerth, 2012). Thus, the interpretation of the observed Ca^{2+} transients is aided by an understanding of the intra- and extracellular sources of Ca^{2+} in neurons. The intracellular Ca^{2+} concentration of neurons is approximately 20-100 nm, with a large concentration gradient from the inside to the outside of the neuron. Ca^{2+} transients corresponding to action potential-related neuronal activity are mainly due to an influx of Ca^{2+} from the extracellular space through voltage-gated Ca^{2+} channels. Other sources of extracellular Ca^{2+} are ionotropic glutamate receptors (Schneggenburger *et al.*, 1993), nicotinic acetylcholine receptors (Rathouz & Berg, 1994), 5HT3 receptors (Nichols & Mollard, 1996) and transient receptor potential type C/TRPC channels (Vazquez *et al.*, 2004). During action potential-related electrical activity, the intracellular Ca^{2+} concentration can rapidly increase by a factor of ten to 100, before it returns to its low baseline Ca^{2+}-concentrations. Besides the cell membrane, Ca^{2+} sources also include intracellular Ca^{2+} stores, which exist in various cellular compartments such as the cell body, dendrites or presynaptic terminals (Grienberger & Konnerth, 2012).

Changes of the intracellular Ca^{2+} concentration influence a broad range of cellular functions, including gene expression, cell proliferation and differentiation (Berridge *et al.*, 2000). Timing and location of changes of the cytosolic Ca^{2+} concentration are highly regulated by endogenous Ca^{2+} buffer protein such as parvalbumin or calbndin-D28k. The concentration of buffer molecules varies in different neuron types. For example, mature cerebellar Purkinje neurons have a particularly high expression level of parvalbumin and calbindin-D28k, resulting in a very high Ca^{2+}-buffering capacity (Fierro & Llano, 1996), while hippocampal parvalbumin-positive interneurons have a comparably lower cytosolic Ca^{2+} buffering capacity (Lee *et al.*, 2000). The Ca^{2+}-buffering capacity and the cell's capacity to remove excess Ca^{2+} from its intracellular space has a crucial influence on the shape and amplitude of fast neuronal Ca^{2+}-transients.

1.3   Ca²⁺-sensitive AM dyes and their limitations

Ca^{2+}-sensitive acetoxymethyl (AM) ester dyes are an efficient and flexible tool to label neuronal populations in the intact brain tissue (Stosiek *et al.*, 2003). They were introduced in the 1980s by Roger Tsien (Tsien, 1981). Upon pressure injection into the brain tissue, the lipophilic AM ester dye molecules diffuse freely through the neuronal lipid bilayer membrane. Once inside a cell, the AM ester groups are cleaved from the dye molecule by endogenous esterases. As a consequence, the dye molecule becomes more hydrophilic and cannot diffuse freely through the cell membrane anymore. Therefore, the dye becomes trapped inside the cell (figure 1.1).

The brightness and photostability of the initially developed dyes have been continuously improved since their first description. Currently used AM dyes such as OGB-1 AM (Stosiek *et al.*, 2003), fluo-8 AM (Busche *et al.*, 2012), and more recently Cal-520 AM (Tada *et al.*, 2014) and Calbryte-520 AM, are used for various imaging applications in many species and brain regions. Most commonly used AM dyes are efficiently excited with wavelengths around 490 nm, or with wavelengths around 920-940 nm for two-photon excitation (Mutze *et al.*, 2012), with emission wavelengths around 520 nm. Attempts to develop dyes with longer excitation wavelengths faced multiple challenges. A low signal-to-noise
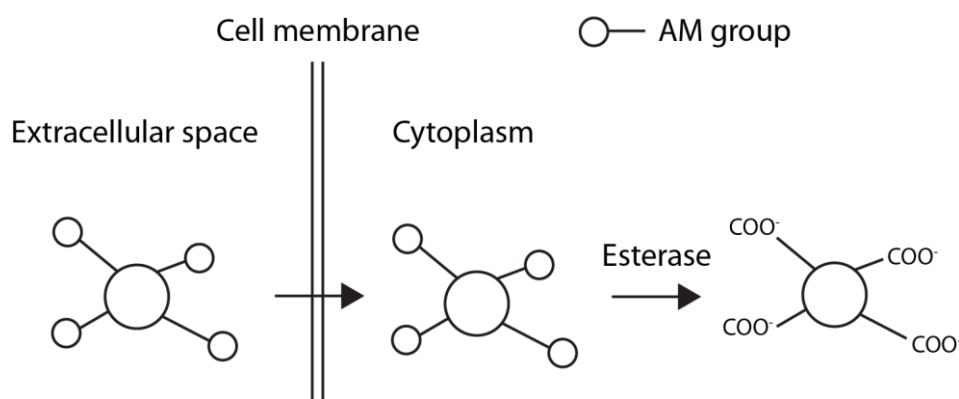
Figure 1.1: Basic principle of labeling cells with AM dyes as described by Tsien, 1981

ratio in the relevant Ca^{2+} concentrations range, slow kinetics, low photostability, low solubility in aqueous solutions, or poor cellular dye retention (see (Oheim *et al.*, 2014) for a thorough review) hindered the applicability of the longer-wavelengths variants of the dyes for in vivo two-photon imaging experiments.

Multiple types of Ca^{2+}-sensitive fluorescent reporters exist (Grienberger & Konnerth, 2012). Besides the synthetic Ca^{2+} indicator this study focuses on, especially genetically-encoded Ca^{2+} indicators have become very useful tools for the analysis of neuronal activity (Chen *et al.*, 2013). Besides their brightness, the possibility to observe Ca^{2+} transients across multiple days opened up new experimental designs, particularly in combination with behavioral tests. Compared to the genetically-encoded probes, advantages of synthetic indicators such as Cal-520 AM (Tada *et al.*, 2014) include the indiscriminate staining of all cells in the brain tissue regardless of their molecular identity (this is beneficial for mapping purposes – the same point would be disadvantage for the study of genetically defined subpopulations of neurons), rapid kinetics, and the possibility to perform acute experiments without long waiting times for gene expression (Stosiek *et al.*, 2003).

1.4 Depth limitation of two-photon microscopy

A major limitation of optical approaches to image neuronal activity with high signal quality is light scattering in opaque brain tissue. While the development of new multiphoton imaging approaches (Ouzounov *et al.*, 2017) and more sensitive Ca^{2+} indicators (Chen *et al.*, 2013; Inoue *et al.*, 2015) allowed for recordings of neuronal activity in the upper layers of the cortex in small mammalian species such as mice or marmosets, neuronal activity typically cannot be recorded in all layers of these brains. The main reason for the depth-limitation of two-photon imaging experiments is light-scattering in the opaque brain tissue (Helmchen & Denk, 2005). Therefore, early experiments in the intact cortex of living mice were commonly limited to layer 2/3 in around 300 µm depth below the cortical surface (Stosiek *et al.*, 2003).

Even with bright, more recently developed fluorophores such as the GCaMP6s (Chen *et al.*, 2013; Li *et al.*, 2015), two-photon imaging of the activity of multiple neurons in local populations remains challenging in deep cortical layers. Out-of-focus fluorescence from densely labeled tissue reduces the optical contrast in underlying imaging regions (Helmchen & Denk, 2005). Therefore, recordings in deep regions are more feasible when recording from isolated, sparsely labeled neurons.

Multiple non-invasive approaches to increase the maximum imaging depth to observe neuronal activity with two-photon microscopy were developed. For example, the use of a regenerative amplifier allowed recordings of Ca^{2+} transients in depths corresponding to layer 5 in the somatosensory cortex (Mittmann *et al.*, 2011). The regenerative amplifier increases the multiphoton excitation-efficiency (at a given average power) of the target fluorophore by increasing the energy per laser pulse. The disadvantage, however, is a reduced laser pulse repetition frequency, which limits the maximum imaging frame rates achievable with such a setup (Mittmann *et al.*, 2011).

Another strategy to image deep in the brain tissue is based on adaptive optics originally used for astronomical observations. In astronomy, aberrations introduced by air masses with varying refractive indices in the Earth's atmosphere have to be corrected (Ji, 2017). For this procedure, the aberration of light from a natural star or a guide star (a laser beam projected into the mesosphere) is measured by a telescope and corrected with a deformable mirror to achieve an optimal optical resolution. Similarly, for two-photon recordings of neuronal morphology or activity in the brain with adaptive optics, the wavefront of the laser beam is deformed with a spatial light modulator to compensate for aberrations introduced by the tissue. With the resulting well-focused laser spot in the tissue, the depth in which a detailed image can be recorded is extended (Ji et al., 2012; Wang et al., 2015).

A very basic approach to extend the two-photon imaging range towards deeper brain structure is the gentle application of pressure to the brain

surface to compress the brain tissue. By shortening the total thickness of the light scattering brain tissue, deeper anatomical structures can be reached for imaging experiments. While the approach can certainly be effective, it can be argued that such a compression changes the micro-architecture of the brain tissue, and is thereby not a purely non-invasive deep-imaging technique. As the technique has mainly been communicated verbally as a welcome byproduct of chronic window implantations used for long-term two-photon imaging experiments, it has not been analyzed systematically so far.

Recently, three-photon excitation (Kobat *et al.*, 2009; Xu & Wise, 2013; Ouzounov *et al.*, 2014) was used to successfully image beyond the cortical tissue in hippocampal CA1 neurons (Ouzounov *et al.*, 2017). In the study, wavelengths around 1300 nm are used to image the bright genetically-encoded Ca^{2+} indicator GCaMP6, which was shown to have a sufficient three-photon excitation cross section to record neuronal Ca^{2+} transients with good signal-to-noise ratios in CA1 pyramidal neurons approximately 1 mm below the brain surface. In general, using longer wavelengths is a straightforward way to image deeper in the intact brain tissue. Compared to commonly used excitation wavelength ranging from 800-940 nm for probes such as OGB-1, Cal-520 or GCaMP6 (Stosiek *et al.*, 2003; Chen *et al.*, 2013; Tada *et al.*, 2014), excitation wavelengths in the range of 1000-1300 nm are more suitable for deep-imaging experiments in the brain, as they are less attenuated in biological tissue (Kobat et al., 2009; Smith et al., 2009; Xu & Wise, 2013). Importantly, fluorophores with longer excitation wavelengths generally also emit light at longer wavelengths, and the emitted photons are also less scattered.

In the wavelength range around 1050 nm, ytterbium fiber lasers are a practical choice to equip two-photon microscopes with (Xu & Wise, 2013; Perillo *et al.*, 2016; Pilz *et al.*, 2016). They have a compact design, requiring less space on the optical table compared to bulkier tunable Ti-Sapphire lasers. Fiber laser models such as the Coherent Fidelity do not require water-cooling, which makes laboratory layouts more flexible and,

important for experiments in the auditory cortex, the laser systems very quiet. Additionally, current fiber laser models can provide femtosecond pulses with very short pulse lengths at high power levels (exceeding 2 W). Finally, they are very cost-effective compared to broadly tunable Ti-Sapphire lasers.

With an increasing imaging depth, the laser power required to achieve a good image quality also increases. It has been estimated that the laser power required for recording an image with similar brightness increases exponentially with the imaging depth (Helmchen & Denk, 2005). At the same time, high levels of laser power cause tissue damage, even at region not in the focal plane. This effect can be particularly harmful to the brain surface above the actual imaging region through which the excitation laser light has to pass, and limits the maximum imaging depth. Thus, it is important to keep the laser power for two-photon imaging experiments as low as possible. Reducing the laser power to avoid photodamage during recordings deep in the intact brain tissue is especially important for experiments with long imaging durations, for example when repeated presentations of sensory stimuli are required.

One factor to increase the efficiency of two-photon excitation, and thereby to decrease the laser power levels necessary for two-photon recordings, is the laser pulse width. The efficiency of two-photon excitation increases linearly with shorter pulse durations (Xu & Webb, 1996). Thus, shorter laser pulse length can contribute to increased imaging depths. Two-photon microscopes are commonly equipped with femtosecond pulsed lasers, which have pulse lengths of, for example, 55 fs (Coherent Fidelity) to 160 fs (Spectraphysics Insight DS+). A comparison of different laser types revealed that for imaging experiments at a depth around 900 µm below the brain surface, only the laser with short pulses of 55 fs required a power level low enough to avoid the risk of photodamage (Birkner *et al.*, 2017).

1.5   Organization of the mouse auditory system

During the past decade, the mouse auditory system has been examined in a wide range of studies (Kanold *et al.*, 2014). For example, the topographic representation of sounds in auditory cortex (Bandyopadhyay *et al.*, 2010; Rothschild *et al.*, 2010; Guo *et al.*, 2012; Winkowski & Kanold, 2013; Issa *et al.*, 2014), thalamus (Hackett *et al.*, 2011) and inferior colliculus (Barnstedt *et al.*, 2015), the subcellular distribution of sound-evoked activity on the level of individual dendritic spines (Chen *et al.*, 2011), development of the auditory system (Barkat *et al.*, 2011), or the involvement of neuronal subtypes for the plasticity of sound-representation in cortex (Kato *et al.*, 2015) have been analyzed. The anatomy of the brain regions involved in auditory processing in mice has
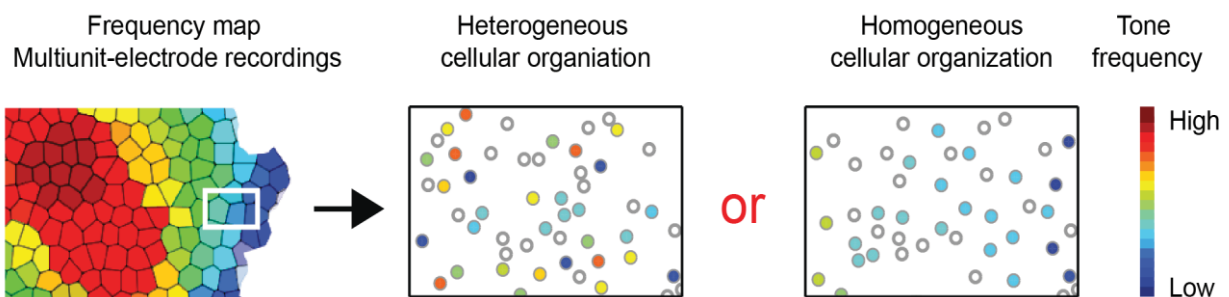
Figure 1.2: Organization of tonotopy in the auditory cortex

Left: Schematic of frequency responses in the entire primary auditory cortex as measured with multi-electrode penetrations (similar to Guo et al., 2012). Each tile indicates one measurement location. The red region corresponds to the high-frequency region of the primary auditory cortex; the blue region corresponds to the low-frequency region. Color scale illustrated on the right.

Middle and right: Illustrations of the magnified region indicated by the white rectangular in the left panel. The region corresponds to a small region within the primary auditory cortex. With single-cell resolution, the spatial arrangement of individual neurons could be either heterogeneous or homogeneous (see Kanold et al., 2014 for details). Color scale illustrated on the right.

been described in great detail (Webster & Fay, 2013). Along the ascending auditory pathway of the mouse, sound information from the cochlea is conveyed to the cochlear nucleus, passes by the superior olivary complex and the lateral lemniscal nuclei to reach the inferior colliculus in the midbrain. It is further transmitted through the ventral division (MGv) of the medial geniculate body (MGB) in the thalamus to the primary auditory cortex and finally to secondary auditory cortex areas.

Indeed, the distinct projections from the medial geniculate body to the primary auditory cortex serve as a well-defined marker to distinguish primary and secondary auditory areas. Primary auditory cortex receives highly organized input from the lemniscal division of the auditory thalamus (medial geniculate body), whereas secondary areas have mainly non-lemniscal thalamical interconnections. Another feature distinguishing primary and secondary auditory cortex is the tonotopic organization of primary auditory cortex, which means that regions responsive to specific tone frequencies are arranged in a gradient-like fashion, with low and high tone-frequencies represented at opposing ends of the area.

Evidence for a location-dependent representation of tone frequencies in auditory cortex has already been shown in the 19th century (Larionow, 1899). During the 20th century, microelectrode recordings made it possible to deepen the analysis of how tone frequencies are organized in the auditory cortex with finer spatial resolution (Merzenich & Brugge, 1973; Andersen *et al.*, 1980). The parcellation of the cat and primate auditory cortex into different subfields, some of which showed a tonotopic organization, was described. Investigation of structures along the auditory pathway showed that the tonotopic organization originates from the frequency-specific activation of hair cells on the basilar membrane of the cochlea, and is preserved along the ascending auditory pathway up to the cortex (Schreiner & Winer, 2007). Using different techniques, including multiunit-microelectrode mapping (Hackett *et al.*, 2011; Guo *et al.*, 2012), and flavoprotein autofluorescence imaging (Tsukano *et al.*, 2017) the tonotopic organization of the mouse primary auditory cortex has been

confirmed on a macroscopic scale. However, the precision of tonotopy on the single-cell level in the cortex remained a matter of debate (figure 1.2, Kanold *et al.*, 2014). Do tonotopic gradients become diffuse and heterogeneous at a very fine scale or does tonotopy persist even on the level of individual neurons?

Using two-photon microscopy, it became possible to address the question for the upper layers of the auditory cortex. Initial results with two-photon Ca^{2+} imaging showed a heterogeneous organization at the single-cell level in layer 2/3 of ketamine-medetomidine anesthetized mice (Rothschild *et al.*, 2010) and isoflurane-anesthetized mice (Bandyopadhyay *et al.*, 2010). It should be noted, however, that the degree of heterogeneity varied in the individual works (Bandyopadhyay *et al.*, 2010; Rothschild *et al.*, 2010; Winkowski & Kanold, 2013; Issa *et al.*, 2014), with two-photon imaging experiments with GCaMP3 mice revealing a high tuning similarity between neurons located close to each other (Issa *et al.*, 2014). In the same work, a higher degree of heterogeneity was found in the secondary auditory cortex compared to the primary auditory cortex. The different results cannot be explained by anesthesia conditions alone, as the heterogeneous spatial organization of neurons in layer 2/3 was later confirmed in awake, head-fixed mice (Li *et al.*, 2017). While the exact reason for the different results between the individual studies remains unknown, we revisited the debate in the course of our effort to map tone-evoked responses in the entire primary auditory cortex.

Interestingly, the degree of heterogeneity observed in the upper cortical layers was reported to be different in layers 2/3 to 4 (Winkowski & Kanold, 2013). A more homogeneous best frequency (BF) organization was described for layer 4 compared to layer 2/3, possibly reflecting the spatial arrangement of thalamocortical inputs. In this work, we aimed to acquire functional data not only for layers 2/3 and 4, but also from the deeper cortical layers 5 and 6 to analyze the tonotopic organization of the auditory cortex in complete, column-like structures, as it has been

speculated that the precision of the tonotopic organization is lower in the deeper cortical layers compared to layer 4 (Hackett *et al.*, 2011).

Beyond the level of individual neurons, improved two-photon imaging methods were used for the investigation of the spatial organization of sound at the subcellular level. A two-photon imaging approach called LOTOS (low-power temporal oversampling) scanning allowed for in vivo recordings of tone-evoked activity of individual dendritic spines (Chen *et al.*, 2011), revealing a heterogeneous organization of postsynaptic BF responses in neighboring dendritic spines. In line with this finding, experiments with genetically-encoded Ca^{2+} indicators injected into the thalamus (ventral section of the medial geniculate body) have shown tonotopically organized axonal inputs into the primary auditory cortex on a large scale, with a heterogeneous organization on the level of individual boutons (Vasquez-Lopez *et al.*, 2017).

Parts of the results focusing on the deep two-photon imaging method have already been published (Tischbirek et al., 2015; Birkner et al., 2017; Tischbirek et al., 2017). The work is cited accordingly, see references for more details.

2.   Aim

The aim of the project was to create a functional map of tone-evoked neuronal activity in all cortical layers of the primary auditory cortex with single-cell resolution. For this purpose, an approach to record neuronal activity with single-cell resolution in all layers of the intact cortex was developed. To **image in the deep layers 5 and 6 of the cortex**, a 'red-shifted' Ca^{2+} indicator was characterized. Next, the deep-imaging approach was combined with conventional two-photon imaging and autofluorescence imaging. The goal was to **map the primary auditory cortex** on two scales, 1: the global brain surface tonotopic gradient and 2: locally distributed neurons throughout the entire depth of the cortex.

Possible insight into the detailed relationship between the orderly tonotopic map spanning the entire primary auditory cortex and the frequency-tuning of neighboring neurons could add to the debate remaining around the representation of tonotopy on the cellular scale, and might add to the understanding of sensory processing in the previously unexplored deep layers 5 and 6.

3. Experimental procedures

3.1. Surgery

All experimental procedures were approved by the state government of Bavaria, Germany, and were performed in accordance with institutional animal welfare guideline. Male and female C57BL/6 mice (postnatal days 30–37) were used. During surgery, anesthesia was induced with isoflurane 1.5% vol/vol in O_2 and continued with MMF (in mg/kg body
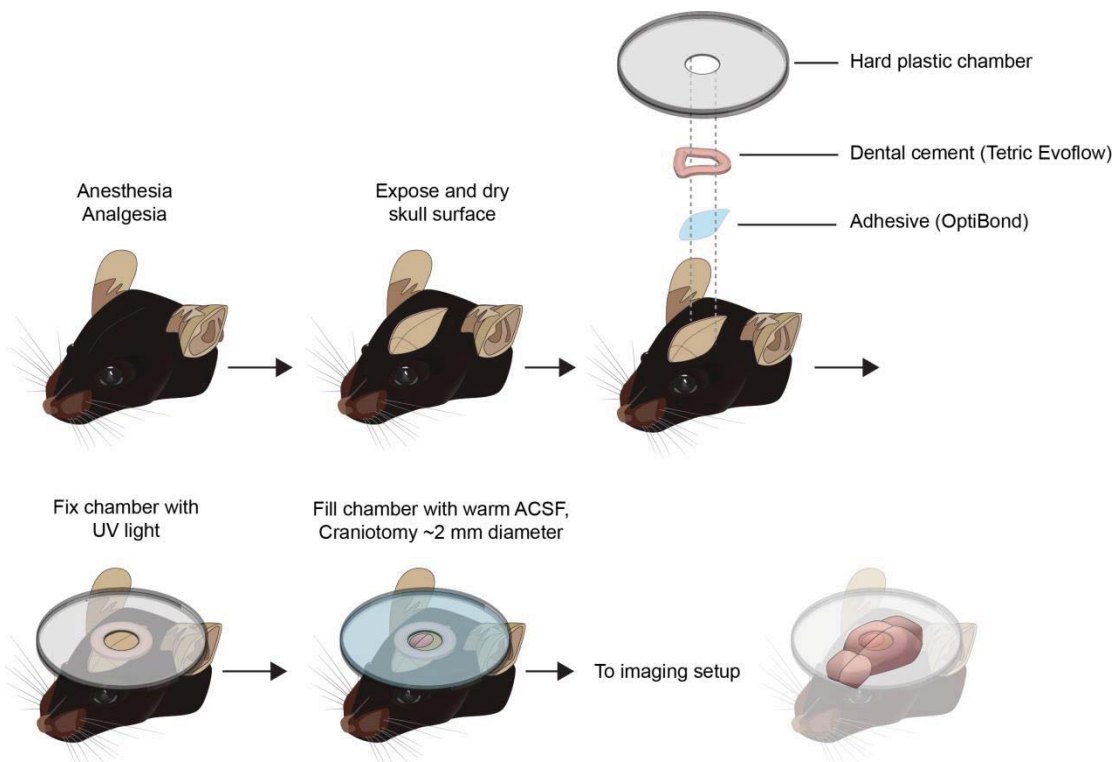
Figure 3.1: Schematic of the procedure used to attach the recording chamber to the skull

The large, solution-filled recording chamber allows for flexible access with glass pipettes for electrophysiological recordings. Note that the procedure is shown for a generic cortical location. The auditory cortex is situated at a more lateral location

weight: medetomidine 0.05, midazolam 0.5, fentanyl: 0.005) for the recording. Mouse vital signs were continuously monitored throughout the entire experiment using biomonitoring equipment (AD Instruments), and the body temperature was set to 37.5 °C with an electronically controlled heating pad. Local anesthesia (2% xylocaine) and analgesia (metamizole, 200 mg/kg) was applied to the operating site, and the skull above the auditory cortex was exposed. A custom-made recording chamber (illustrated in Figure 3.1) was attached to the cleaned skull using a light-curing bonding agent (OptiBond All-in-One) and resin-based dental cement (Tetric EvoFlow). A craniotomy was performed above the auditory cortex, which was localized using flavoprotein autofluorescence imaging. 2% agarose (Sigma-Aldrich, dissolved in distilled H_2O or 0.9% NaCl solution using a standard microwave) was applied to stabilize the exposed brain surface. MMF was re-injected at controlled time intervals to maintain the appropriate depth of the anesthesia. The craniotomy was continuously superfused with 37.5 °C solution containing, in mM, 125 NaCl, 4.5 KCl, 1.25 NaH_2PO_4, 26 $NaHCO_3$, 2 $CaCl_2$, 1 $MgCl_2$, 20 glucose. Carbogen gas was bubbled into the solution to set its pH value to 7.4. The temperature of the solution was continuously monitored with a water-proof thermometer (AD instruments). The flow of the solution was maintained at a constant speed with a peristaltic pump.

3.2. Flavoprotein autofluorescence imaging of the brain surface

Transcranial autofluorescence signals (Takahashi *et al.*, 2006) were recorded in a dedicated imaging setup illustrated in figure 3.2. It consisted of a binocular microscope (MVX10, Olympus), a 0.63 x, 0.15 NA objective (MV PLAPO, Olympus), an Olympus U-M49002XL filter cube (excitation filter: 470/40 nm, dichroic mirror: 495 nm high pass, emission filter: 525/50 nm) and a CMOS camera (Zyla 4.2 Plus, Andor). To increase bone transparency, the skull surface was covered with 0.9 % NaCl solution. To excite flavoprotein fluorescence, we used a 470 nm LED (M470L2-C1, Thorlabs) at an intensity level of 4.2 mW below the objective. Images (128 x 128 pixels, 10 Hz sampling rate) were recorded using custom-written acquisition software (LabVIEW 2014, National Instruments).
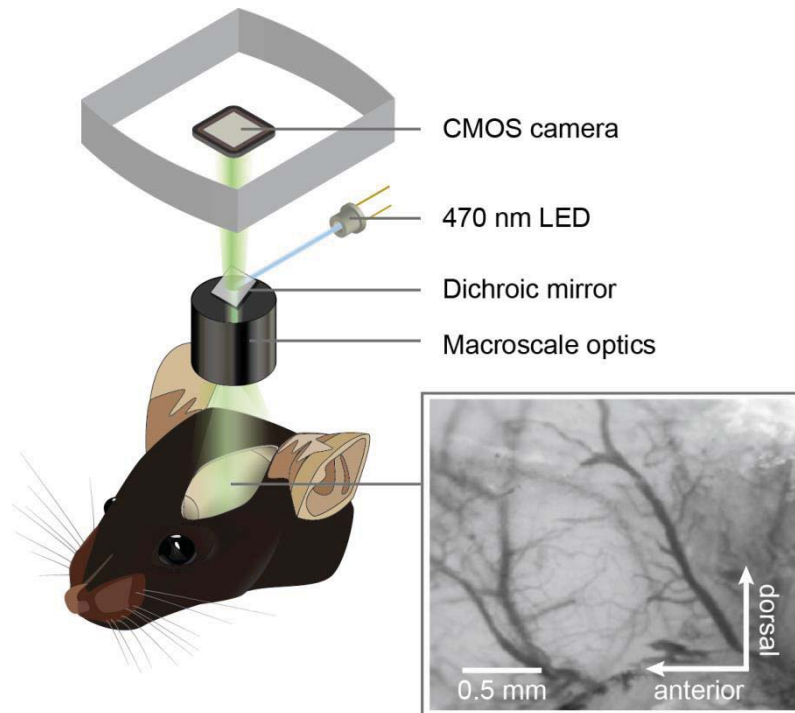
Figure 3.2: Illustration of the CMOS-camera based imaging setup to measure autofluorescence signal through the intact skull

Bottom right: An example autofluorescence image of the skull surface is shown. The dark pattern within the image corresponds to blood vessels.

3.3. Two-photon imaging setup and imaging parameters

During the course of the project, numerous pulsed lasers were tested for in vivo two-photon Ca^{2+} imaging in deep cortical layers. Best results were obtained with a combination of two lasers, that were used interchangeably on the setup: A pulsed fiber laser fixed at a wavelength of 1070 nm with a pulse width of 55 fs (Fidelity, Coherent) and a tunable pulsed infrared laser (InSight DeepSee, Spectra-Physics or Coherent Discovery, Coherent) for recordings with wavelengths ranging from 920-1200 nm and laser pulse widths below 120 fs. To switch between both lasers, an electrically movable mirror (Thorlabs) was used. We used a Conoptics Model 302

laser modulator to control the laser intensity, and a beam expander to adjust the laser spot size (BE02M-B; Thorlabs). In the custom-built scanner box, a resonant scanning mirror with a resonance frequency of 12 kHz and a standard galvanometric mirror (Cambridge Technology) were used to scan the fast and slow image axis, respectively. The scanning beam entered the chassis of the microscope (Olympus, BX51WI) through a scan-lens optimized for wavelengths up to 1050 nm (AC508150BML, Thorlabs), which was, however, still suitable for the longer laser wavelengths used here. A dichroic mirror (F73-705, AHF Analysentechnik, reflecting 710-1500 nm) was used to reflect the scanning beam onto the sample. Emission photons were transmitted through the dichroic (400-680
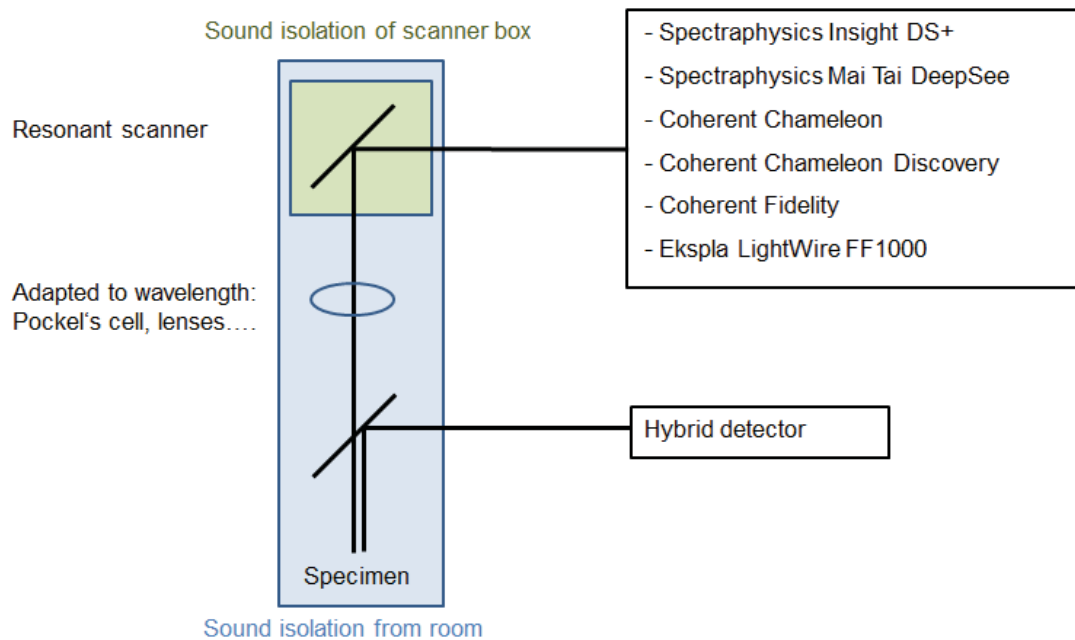
Figure 3.3: Illustration showing the basic configuration of the two-photon microscope

Multiple lasers (listed on the top right) were tested, before the final configuration using the Coherent Fidelity and Coherent Chameleon Discovery was chosen. The resonant scanner box was inside the sound isolation box surrounding the microscope, and therefore required an additional sound isolation box. See text for technical specifications of individual components.

nm) through a short-pass emission filter (cut-off frequency 680 nm) onto the detector. The maximum laser power under the water-immersion objective (40 x, NA 0.8, Nikon Corporation) used in the deepest cortical regions did not exceed 120 mW. Depending on the configuration of the experiment, one or two hybrid photo detectors R7110U-40 (Hamamatsu) with a DHPCA-100 amplifier (FEMTO Messtechnik GmbH) were used to detect fluorescence signals. For two-channel recordings, the detectors were separated by an additional suitable dichroic mirror. The microscope was controlled by custom-written software (LabVIEW 2014, National Instruments).

The two-photon imaging setup was specifically built for auditory stimulation experiments (see figure 3.3). To allow for suitable recording conditions for acoustic stimulation experiments, acoustic noise from the imaging hardware and peripheral experimental equipment had to be reduced. Moving the laser cooling unit of the tunable laser to a separate room improved the acoustic noise level in the experimental room. A sound-attenuation cage was custom-built to reduce the noise level below 20 dB in the relevant sound frequency range. The laser scanner remained as a source of acoustic noise from within the sound attenuation cage. Its noise was reduced to below 20 dB SPL with additional metal casings and multiple layers of sound-dampening materials around the scanner box.

Images of neuronal populations were acquired at 40 and 80 Hz. Dendritic Ca^{2+} transients were recorded with 200 Hz (or 500 Hz if noted in the specific data set). For each imaging region, a z-stack projection was recorded to verify and document the recording depth below the brain surface. Cortical layers were defined according to depths from anatomical (Anderson *et al.*, 2009) and functional data (Christianson *et al.*, 2011).

3.4. Dye loading procedure

The procedure described here is based on the multi-cell bolus loading approach (Stosiek *et al.*, 2003), which was modified to label neurons all

layers of the cortex. 50 µg Cal-590 or Cal-520 AM (both AAT Bioquest) were dissolved in 4 µL DMSO + 20% pluronic-127. The dye was dissolved to 500 µM in solution containing, in mM, 150 NaCl, 2.5 KCl, 10 Hepes at pH 7.4 as illustrated in figure 3.4. 25 µM Alexa680 (Sigma) was also included in the solution to enable two-photon guidance during the staining procedure. 3-5 MΩ borosilicate glass pipettes (Hilgenberg GmbH) were made using a vertical puller (PC-10; Narishige Co., Ltd.) and backfilled with 5-10 µl dye solution (figure 3.5).
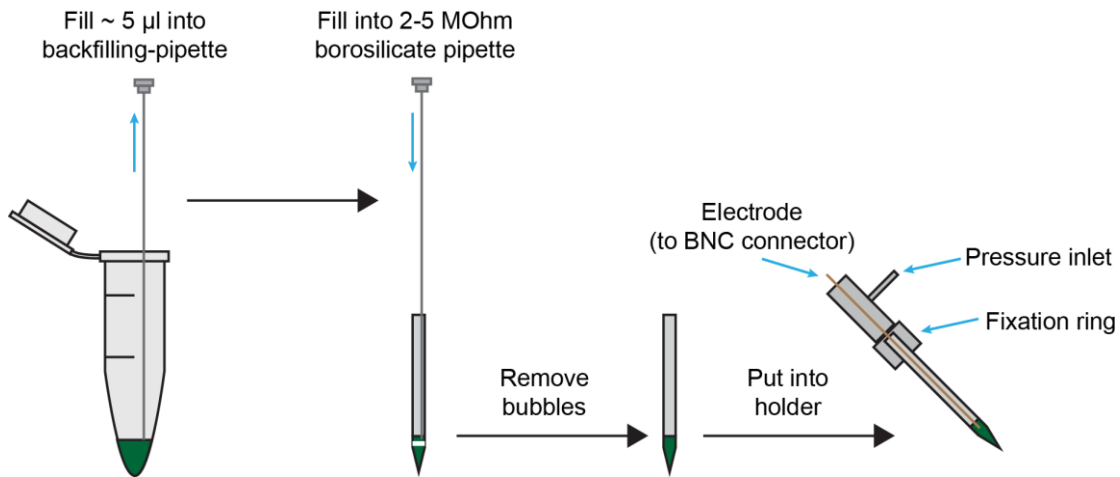
To facilitate labeling in deep cortical regions, the pipette was angled as steep as possible (34-37°). The maximum angle was limited by the size and working distance of the microscope objective, as the pipette tip had to be visible for two-photon guidance. The position of the pipette was
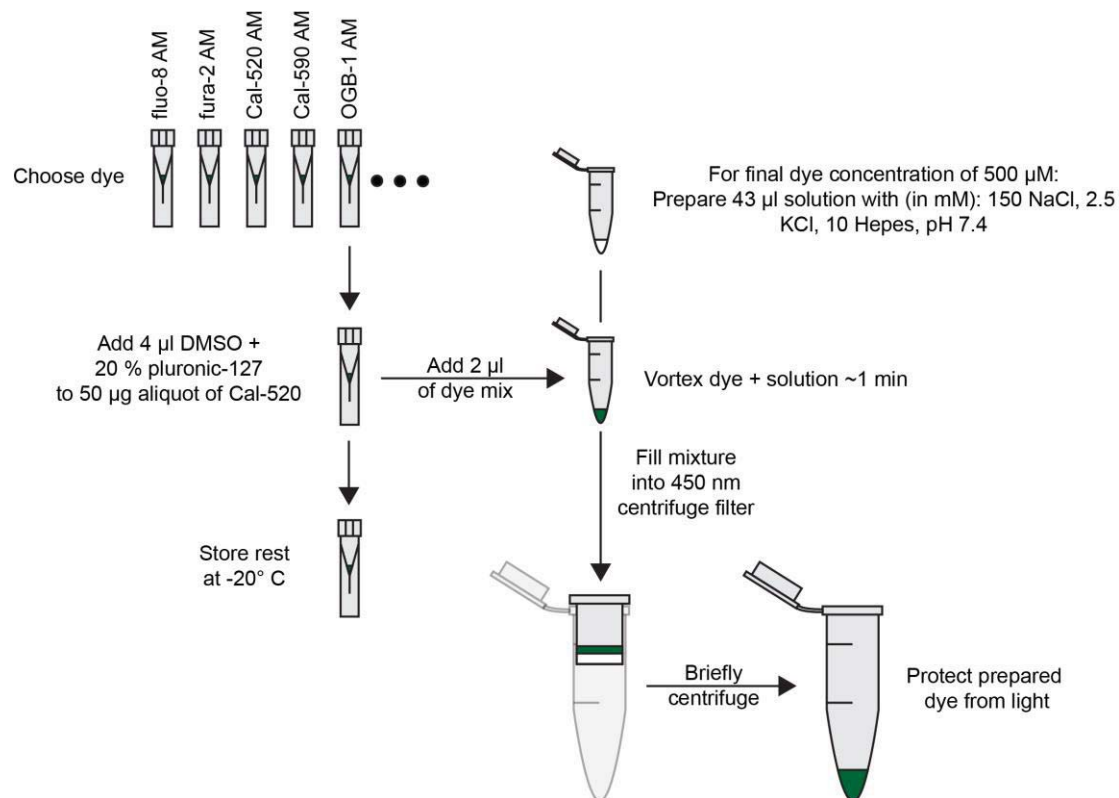
Figure 3.4: Illustration of the preparation workflow for AM dyes used for pressure injection into the intact brain tissue

The amount of solution noted to reach 500 µM is based on the molecular weight of Cal-520 AM.

Fill ~ 5 µl into backfilling-pipette

Fill into 2-5 MOhm borosilicate pipette

Remove bubbles

Put into holder

Electrode (to BNC connector)

Pressure inlet

Fixation ring

Figure 3.5: Schematic showing the detailed steps necessary to prepare the injection pipettes used for the in vivo loading procedure
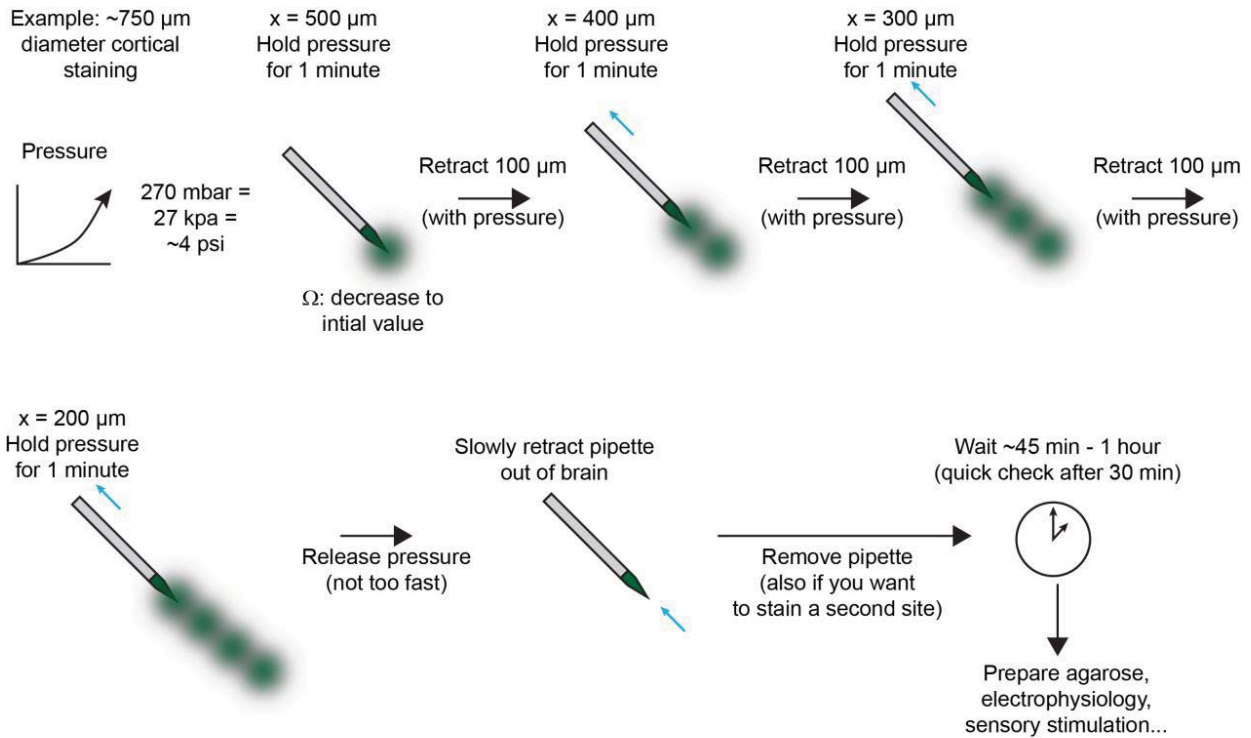
controlled with a micromanipulator (Luigs + Neumann) and carefully inserted into the brain (figure 3.6). Pipette movements other than along its longitudinal axis were avoided to prevent tissue damage. To eject dye solution from the pipette, pressure was manually applied and monitored with a pressure meter (50-150 mbar, figure 3.7). Rapid pressure changes were avoided to prevent brain tissue damage. Alexa680 fluorescence was monitored to control the size of the labeled region, which was especially important to avoid out-of-focus fluorescence in deeper cortical layers

Ω: initial value

Ω: increase

Ω: further increase

Ω: decrease
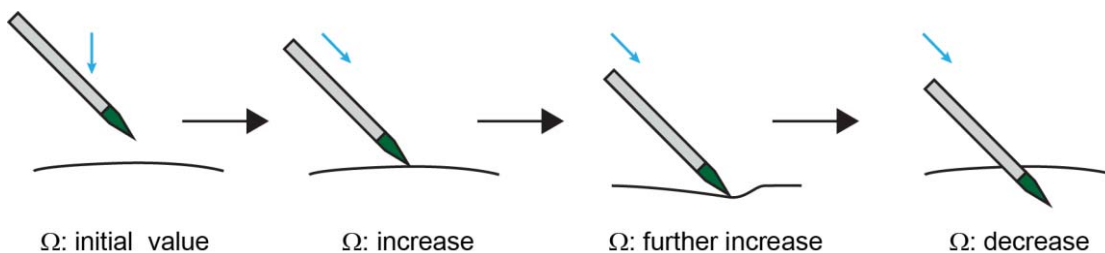
Figure 3.6: Illustration showing the penetration of the dura with the injection pipette

The pipette resistance is monitored continuously during the injection. Blue arrows indicate the movement direction of the pipette controlled by a micromanipulator.

Example: ~750 µm diameter cortical staining

Pressure

270 mbar = 27 kpa = ~4 psi

x = 500 µm Hold pressure for 1 minute

Ω: decrease to intial value

Retract 100 µm (with pressure)

x = 400 µm Hold pressure for 1 minute

Retract 100 µm (with pressure)

x = 300 µm Hold pressure for 1 minute

Retract 100 µm (with pressure)

x = 200 µm Hold pressure for 1 minute

Release pressure (not too fast)

Slowly retract pipette out of brain

Remove pipette (also if you want to stain a second site)

Wait ~45 min - 1 hour (quick check after 30 min)

Prepare agarose, electrophysiology, sensory stimulation...

Figure 3.7: Illustration of pressure injection method

Shown here is the procedure to label a large area of the brain (with multiple injections). Green shapes indicate fluorescent dye. For targeted loading, only one injection is performed, and the injection time and pressure are adjusted according to the feedback from real-time two-photon imaging data (see text for details).

(Birkner *et al.*, 2017). Imaging was performed 1 hour after the loading procedure. If a larger stained area was necessary, the procedure was repeated with subsequent labeling sites either above or next to the original imaging location as illustrated in figure 3.7.

3.5. Electroporation of individual neurons

The solution used for electroporation of single L5 neurons contained, in mM: 1 Alexa680 or Alexa594 (Sigma) 135 K-Gluconate, 4 KCl, 10 Hepes, 10 Na_2Phosphocreatine, 4 Mg-ATP, 0.3 Na-GTP at pH 7.4. The solution

was backfilled into a borosilicate glass pipette with a resistance of 5–7-MΩ. Under two-photon guidance, the pipette was navigated to the target neuron. In the experimental configuration used here, the cells were already labeled with Cal-590 AM in a previous step, and therefore readily identified using two-photon imaging. With the target cell in close proximity to the pipette tip, two squared current pulses (270 nA, 30 ms) were applied to the pipette with a custom-built amplifier and a pulse stimulator (Isolated Pulse Stimulator Model 2100, A-M Systems) or an npi amplifier (ELC-01MX and TMR-02M, npi electronic GmbH). The pipette was retracted, repositioned, and used to electroporate neighboring neurons. 30 minutes after electroporation, the dye had diffused sufficiently within the target neuron to record two-photon z-stack projections for posthoc reconstructions of the cell's morphology. For electroporation of individual neurons with Ca^{2+} indicator dyes, Cal-590 K+ or OGB-1 salt were dissolved to 9 mM in the solution described before. The pipette was navigated in the brain tissue using the shadow-patching approach (Kitamura et al., 2008), and Ca^{2+} transients were recorded after waiting for at least 1 hour after the electroporation.

3.6. Electrophysiology

Patch-clamp recordings in the cell-attached configuration were made with an EPC9 amplifier (HEKA). A borosilicate glass pipette (resistance 5 and 6 MΩ) was filled with 12.5 or 25 µM Alexa Fluor 594 dissolved in solution containing, in mM: 125 NaCl, 4.5 KCl, 1.25 NaH2PO4, 26 NaHCO3, 2 CaCl2, 1 MgCl2, 20 Glucose, pH 7.4. The pipette was inserted into the brain and guided to the target neuron with the shadow-patching approach similar to the electroporation procedure (Kitamura et al., 2008). A seal of 20-50 MΩ with the target neuron was established.

A pair of silver ball surface electrodes from the dorsal neck muscles was used to record EMG signals. For data acquisition, EMG signals were amplified with an AC amplifier (100 x gain, npi Electronic) and digitized at 12 kHz. A digital bandpass filter (20 to 200 Hz) was applied to the recordings.

3.7. Auditory stimulation

Pure tones for auditory stimulation were generated and controlled using custom-written software (LabView). An electrostatic loudspeaker driver and loudspeaker (ED1, PA5, Tucker Davis Technologies) was placed ~5 cm from the contralateral mouse ear to present acoustic stimuli to the mouse. During flavoprotein autofluorescence imaging, sequences of six pure tone bursts (100 ms duration with 10 ms on and off linear ramps, 200 ms inter-stimulus interval, 55 dB SPL) with 4 and 32 kHz were presented alternatively 20 times to localize A1. Sequences had a 10 second interval between them. To characterize tone-evoked responses of neurons during two-photon imaging experiments, randomly ordered pure tones with 19 different frequencies (2–45.3 kHz) were used. Tones had 5 different attenuation levels (20–70 dB SPL), resulting in a total of 95 frequency-attenuation combinations. Stimulation sequences consisted of pure tones with 100 ms duration (including 10 ms on and off linear ramps), and an inter-tone interval of 1500 ms. Each frequency-attenuation combination was presented 8-10 times.

3.8. Data analysis

Data analysis was performed with custom-written software using LabVIEW 2014 (National Instruments) and MATLAB version R2013a and R2014b (Mathworks).

3.8.1. Autofluorescence imaging data

For each pixel, the average ΔF/F value of 10 frames (starting 5 frames after stimulation onset) was divided by the average ΔF/F value of 10 frames before the stimulation. The calculation was repeated for all 20 trials of each stimulation conditions, and an average image of all trials was calculated for each condition. The resulting images were filtered with a Gaussian filter with a 7 pixel diameter. To estimate the A1 tonotopic axis, the center points of the regions responding to 4 and 32 kHz tone stimulation were connected. The corresponding brain surface tone

frequency along the tonotopic axis was determined by spatial linear interpolation.

3.8.2. Two-photon imaging data processing

Manually selected regions of interest (ROIs) were used to extract Ca^{2+} traces from raw imaging data. Time series for a cellular ROI were created based on the ROI's average fluorescence value in each recorded frame. To correct for fluctuating background fluorescence values, each cellular ROI was surrounded by a second, donut-shaped ROI. For the second ROI, the average fluorescence value was calculated, multiplied with a contamination ratio (Kerlin *et al.*, 2010; Hagihara *et al.*, 2015), and subtracted from the cellular ROI. The ΔF/F value was calculated for each frame, with baseline fluorescence F = 10% of the non-parametric z-score series of a 31 second time series for each ROI. The resulting time course was low-pass filtered by a finite impulse response filter (designed by the Parks-McClellan algorithm of the MATLAB function 'firpmord'). The pass and stop frequencies of the filter were 22 and 12 Hz. An additional bandstop-filter was applied (9.5 - 10.5 Hz). To avoid distortion of the temporal features of the Ca^{2+} transients, zero-phase filtering was used (MATLAB function 'filtfilt').

3.8.3. Active ROIs

'Active' neuronal ROIs were defined as neurons that showed a significant Ca^{2+} transient at any time point during the recording, regardless of whether it is spontaneous or stimulation-dependent. To detect such a ROI, the ΔF/F time course was high-pass filtered (0.4 Hz) to remove any slow trends. It was then normalized using the median and MAD of the ΔF/F distribution. In the normalized time series, ΔF/F peaks were detected with the MATLAB function 'findpeaks'. As a first selection criterion, Ca^{2+} transients were accepted as 'active' if the peak normalized scores were >3.45 (corresponding to a z score of 2.33) and if the normalized difference between onset time and peak time was greater than 2. The onset of a Ca^{2+} transient was the time interval between the last trough

before the peak and the peak. As a second selection criterion to detect 'active' ROIs, peak and decay integral ΔF/F values were determined (Rothschild *et al.*, 2010). Peak ΔF/F was calculated as the difference of ΔF/F between Ca^{2+} transient onset and the peak value. Decay integral ΔF/F was defined as the time integral of ΔF/F values from the peak time to 300 ms thereafter. Peak and decay integral ΔF/F distributions of each ROI were converted into normal distributions by a Box-Cox transformation (exponents $\lambda = 0.75 \pm 0.40$ and $\lambda = 0.27 \pm 0.75$ for peak and decay integrals). A neuronal ROI was considered 'active' (during at least 900 s recording time) when at least one event in the transformed ΔF/F distribution of Ca^{2+} transients was ≥ 25 Mahalanobis distances from the ΔF/F values in a selected "inactive" neuropil/blood vessel ROI.

3.8.4. Responsiveness to pure tones

The average prestimulus baseline ΔF/F value (time interval: -300-0 ms) was subtracted from the average poststimulus peak ΔF/F value (time interval: 20-320 ms) of all trials to calculate the amplitude of tone-evoked Ca^{2+} transients. A ROI was defined as "responsive" if a tone-evoked Ca^{2+} transient had a statistically significant ΔF/F value ($p < 0.05$) as determined by a one-way ANOVA of all 95 frequency-attenuation conditions.

3.8.5. Analysis of frequency response areas

The frequency response area (FRA) of a ROI is based on the analysis of all 95 frequency-attenuation combinations, and groups together all responsive frequency-attenuation conditions. To determine the responsiveness of a frequency-attenuation condition, two criteria were used: the response had to show a significant change of the poststimulus signals from prestimulus signals (Wilcoxon's signed rank test, $P < 0.05$), and the response had to occur in at least 30% of the trials. A response was considered to occur in a single trial when the poststimulus time-averaged signal was at least 3 standard deviations higher than the pre-stimulus baseline. Tuning curves representing the FRA boundaries were

based on the edges of the responsive frequency-intensity conditions, showing adjacent responsive and non-responsive frequency-intensity combinations. All FRAs were inspected visually to check their plausibility, showing that the analysis procedure resulted in clear FRA boundaries in 85% of the cases. To calculate the best frequency (BF) of a ROI, the responses of all attenuation levels was averaged for each frequency. The frequency condition with the maximum averaged ΔF/F value was the BF. The d' (Guo *et al.*, 2012) value was calculated as a measure for the signal quality of the FRAs across the different layers. The minimum intensity threshold was the highest attenuation where a significant ΔF/F value was observed. The sharpness of the FRA and its bandwidths at different attenuation levels above the minimum threshold were also determined from the tuning curve.

3.8.6. Analysis of BF distribution

The BFs of individual neurons were analyzed and their distribution within fixed-size analysis windows determined (200 μm x 130 μm). For the comparison of the BF heterogeneity between cortical layers, the range covering 90% of the data points (R_{90}) and the inter-quartile range of the distributions were calculated (Winkowski & Kanold, 2013).

3.8.7. Alignment of imaging data from different layers

The dendritic trunk axis of electroporated L5 neurons was used to align imaging regions recorded in separate layers. See figure 3.8 for a schematic of the alignment. The vector along the dendritic trunk axis of the L5 neurons was defined based on the direction of at least 3 different dendrites in one imaging region. The coordinates to calculate the vectors were extracted from two-photon z-stack recordings with the ImageJ Plugin Simple Neurite Tracer (Longair *et al.*, 2011). Imaging regions not overlapping with their adjacent layers were not included in the analysis of tone-response properties across different layers.
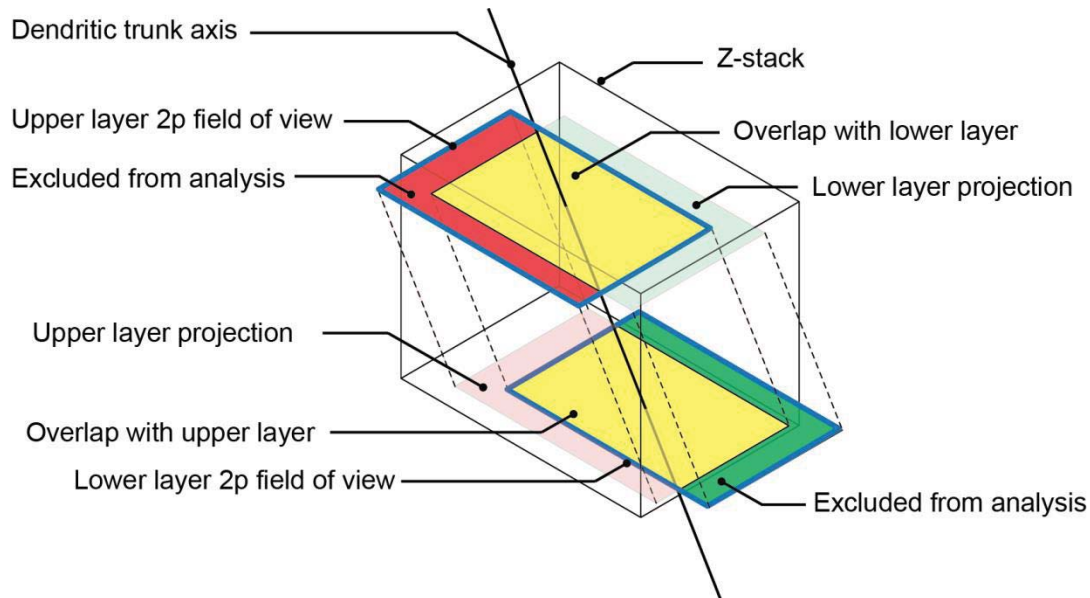
Figure 3.8: Schematic of the alignment of two adjacent layers

Red: Two-photon imaging plane of the upper of two adjacent layers. Green: Two-photon imaging plane of the lower of two adjacent layers. Yellow region shows the overlapping region included in the data analysis. Cells outside of the yellow region were excluded from the analysis. See text for details.

3.8.8. Micro-tonotopy

To determine the tonotopic axis on the level of individual neurons within local regions, a BF gradient vector (Guo *et al.*, 2012) was calculated for each pair of frequency-tuned neurons. The BF gradient vector was defined as the BF difference between the neurons normalized by the Euclidean distance between their locations, multiplied by a unit vector directed from the location of the first to the second neuron. All BF gradient vectors in the fixed-size imaging field of view (with at least 7 neurons) were averaged to define the axis of the "micro-tonotopic gradient"

3.8.9. Significance of BF change

The distance along the tonotopic and isotonotopic axis necessary for a significant BF change of a local population of neurons was measured. First, two separate analysis windows were defined for the analysis region. The analysis windows had a fixed (130 µm orthogonal to the tested axis) and a variable side length (30-90 µm parallel to the tested axis). The distance between the two analysis windows increased in 10 µm steps. The BF distribution of all individual neurons within each analysis window was determined. Using a two-sample t-test, the difference between the means of the distributions of both analysis windows was tested. Next, the median distance necessary to reach a significant BF difference between the two analysis windows was determined. To reduce the impact of the analysis window size, the procedure was repeated for window sizes from 30 to 90 µm.

3.8.10. Image processing

For illustrative purposes only, the contrast of two-photon average images was homogeneously adjusted with ImageJ. Skull surface images were overlaid with autofluorescence imaging data with Adobe Photoshop CS5. Amira 6.0 (FEI, Thermo Fisher Scientific) was used for the visualization of dendritic reconstructions from z-stack projections.

4.   Results

4.1   Autofluorescence imaging to localize primary auditory cortex

We used flavoprotein autofluorescence imaging to create a brain surface map of sound-evoked neuronal activity in the auditory cortex. The map served two purposes. First, it was used to clearly identify primary auditory cortex in each experiment, which is ~500 µm wide and cannot be localized based on anatomical markers such as blood vessels or bone patterns. Secondly, the map was an integral component of our analysis to relate the brain surface tonotopy with cellular activity patterns observed in every experiment. For both purposes, an inherent advantage of autofluorescence imaging compared to other fluorescence-based localization methods (Issa *et al.*, 2014) is the lack of additional fluorescent dyes or marker molecules that have to be introduced into the brain tissue. Any additional fluorescent marker might decrease the imaging quality for the two-photon imaging performed at the later stages of the experiment.

The setup illustrated in figure 3.2 was used for stable autofluorescence recordings. Previous reports have shown that various kinds of sound and a large number of tone frequencies can be used to create a detailed map of the different subfields of the entire auditory cortex (Takahashi *et al.*, 2006). We observed tone-evoked fluorescence changes for a variety of sounds, for example to bursts of pure tones with 45.3 kHz (figure 4.1). For a reliable mapping procedure in every mouse, we used a combination of pure tones with 4 and 32 kHz to resolve the tonotopic gradient of the primary auditory cortex (figure 4.2). Local increases of autofluorescence intensity corresponded to the low and high frequency regions of the primary auditory cortex, which were activated by stimulation with 4 and 32 kHz, respectively. The axis of the tonotopic gradient was defined based on the center-points of the responding regions (figure 4.2).
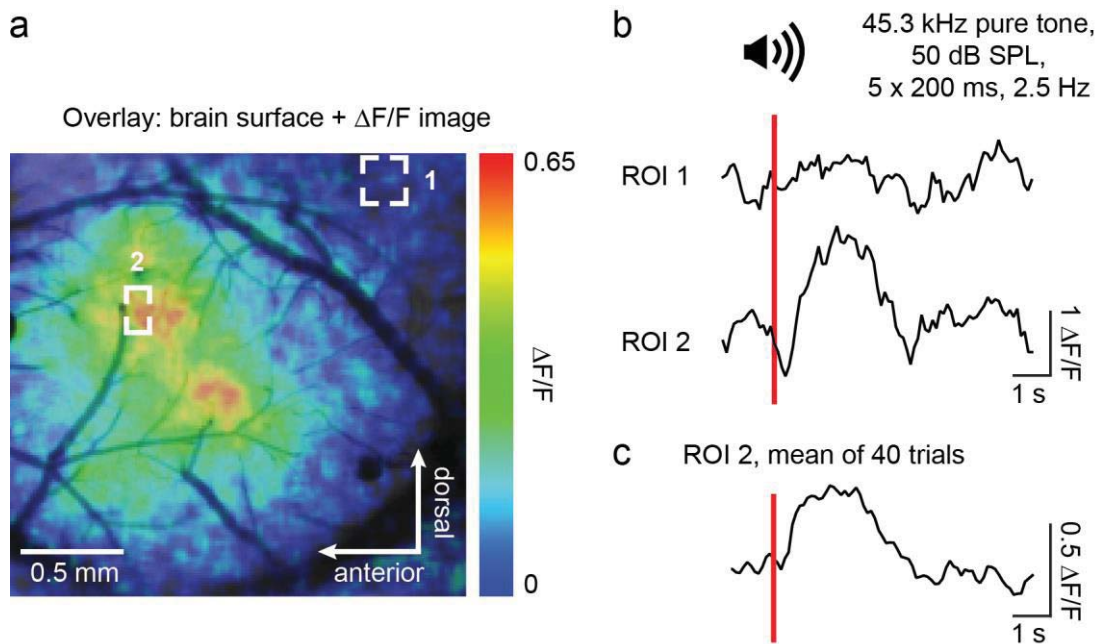
Figure 4.1: Autofluorescence signals in response to pure-tone stimulation imaged through the intact skull in the primary auditory cortex

a. Example recording showing an overlaid image of the brain surface and the color-coded autofluorescence response during pure tone stimulation with 45.3 kHz.

b. Black trace: Time courses of the autofluorescence signal of two example regions of interest (ROI) as indicated by white rectangles in panel a. Traces for a single stimulation are shown. ROI 1 corresponds to a weakly responding region, ROI 2 to a strongly responding region. Red line indicates the time point of pure-tone stimulation.

c. Like panel b, but for the averaged time course of 40 stimulation trials presented to the mouse and measured at ROI 2.
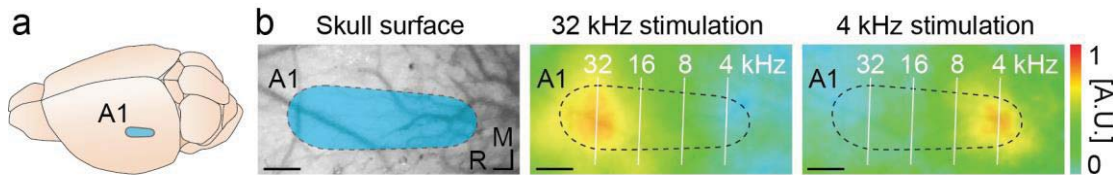
Figure 4.2: Localization of the primary auditory cortex through the intact skull with functional flavoprotein autofluorescence imaging

a. Schematic of the adult mouse brain. Location of the primary auditory cortex (A1) is indicated by the blue patch.

b. Left panel: Skull overlying the left auditory cortex. A1 is indicated by the blue patch. Right panels: Brain surface imaging example, showing the autofluorescence response during pure tone stimulation with 32 kHz and 4 kHz. Black dotted line indicates A1 boundary. Scale bars: 200 µm.

4.2 Spectral properties of Cal-590

As the aim of this work was to map auditory responses in all layers of the cortex, we set out to image neuronal responses throughout the entire cortical depth down to deep layer 6 around 1000 µm below the brain surface. However, most conventional two-photon imaging approaches are limited to recording depths around 500 µm. To extent the maximum imaging depth, we used the recently developed Ca^{2+} indicator Cal-590, which has excitation and emission wavelengths advantageous for deep imaging experiments (Zhao *et al.*, 2015). We measured the spectral properties of Cal-590 to determine which wavelengths are most suitable for two-photon excitation of the dye (figure 4.3). Based on the single-photon excitation spectra made available by the supplier of Cal-590 (AAT Bioquest, Sunnyvale USA), it was known that the dye has a longer excitation wavelength compared to the recently tested Ca^{2+} indicator Cal-520 (Tada *et al.*, 2014), which has its optimum two-photon excitation wavelength around 920 nm. In our measurements (Tischbirek *et al.*, 2017), we found the maximum for two-photon excitation of Cal-590 at
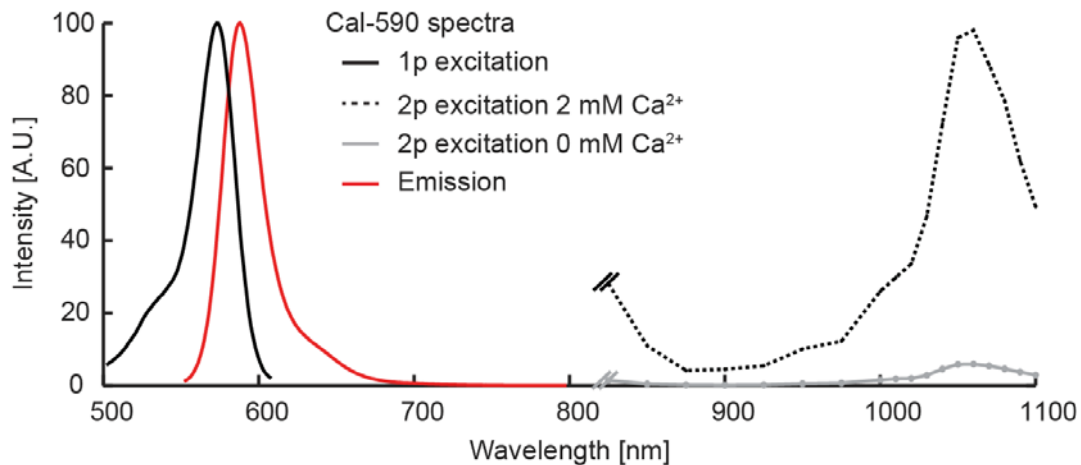
Figure 4.3: Emission and excitation spectra of Cal-590 with 0 and 2 mM Ca^{2+}. Figure modified from Tischbirek et al., 2017

Graph shows the normalized single-photon (1p) and two-photon (2p) excitation spectra as well as the emission spectrum of Cal-590. Two-photon spectra are shown with and without Ca^{2+}. Single-photon spectra adapted from AAT Bioquest (Sunnyvale, USA).

wavelengths around 1050 nm (black dotted line, figure 4.3). At this wavelength, the attenuation length in the brain tissue is reduced compared to, for example, 920 nm (Kobat *et al.*, 2009; Sordillo *et al.*, 2014), thus permitting two-photon imaging experiments deeper in the intact brain tissue.

4.3 Two-photon Ca^{2+} imaging with Cal-590

To test the performance of the dye for in vivo two-photon Ca^{2+} imaging experiments, we used Cal-590 AM to label a local population of cells in cortical layer 2/3 of the visual cortex. The AM version of the dye was pressure injected into the intact brain tissue (Stosiek *et al.*, 2003). The resulting staining pattern of Cal-590 showed a brighter neuronal cytosol compared to the nucleus (figure 4.4a). Time courses recorded from the neuronal somata revealed Ca^{2+} transients, which we analyzed in more
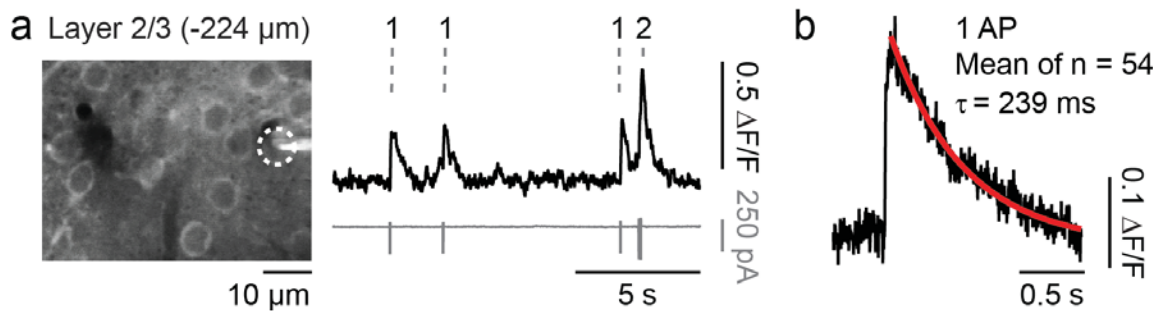
Figure 4.4: *In vivo* two-photon Ca^{2+} imaging of neuronal populations in cortical layer 2/3 with Cal-590 AM. Figure modified from Tischbirek et al., 2015

a. In vivo two-photon image (left, average of 30 s recording time) of cortical layer 2/3 neurons. Ca^{2+} transients (right) were measured in the region indicated by the white dotted line. Cell-attached recordings were made in parallel from the same cell. The number of action potentials is indicated above the cell-attached recording (bottom grey trace).

b. Averaged Ca^{2+} transient recorded during 54 single action potential events in three different animals. Red line indicates a single exponential fit to the trace.

---

detail with parallel patch-clamp recordings in the cell-attached configuration. We observed that it was possible to record Ca^{2+} transients associated with single action-potential events with a good signal-to-noise ratio (figure 4.4b) despite Cal-590's lower Ca^{2+} binding affinity compared to, for example, OGB-1 (K$_d$ Cal-590 = 561 nM, K$_d$ OGB-1 = 170 nM). The single action potential-related Ca^{2+} transients had rapid rise (< 2 ms) and decay times. High quality recordings of Ca^{2+}-transients with Cal-590 AM were possible for at least 2-3 hours after the staining procedure. Taken together, Cal-590 AM is suitable as a sensitive reporter of neuronal population activity with single-cell resolution *in vivo* (Tischbirek *et al.*, 2015).

4.4 Recording Ca^{2+} transients from individual neurons with Cal-590

When the potassium salt version of Cal-590 is used instead of Cal-590 AM, the dye cannot freely diffuse through the lipophilic cell membrane. Thus, it is not feasible to label a group of neurons with Cal-590 potassium salt with the same pressure-ejection approach used for AM dyes (Stosiek *et al.*, 2003). Instead, pressure ejection of Cal-590 potassium salt mostly stains the extracellular space. However, other approaches to deliver hydrophilic dyes like Cal-590 potassium salt to the intracellular neuronal space have been developed. For example, the dye can be dialyzed using a whole-cell patch-clamping approach. Another technique is single-cell electroporation, which was used here to stain individual neurons with Cal-590 potassium salt.

A target cell in L5 of the mouse visual cortex was approached using the shadow-patching approach (Kitamura et al., 2008) under constant visualization with the two-photon microscope. Figure 4.5a shows an example reconstrution of a neuron based on a two-photon z-stack projection reocrded one hour after labeling by single-cell electroporation. In the electroporated neuron, action potential-associated Ca^{2+} transients had much more rapid decay time-courses in the dendrites than in the cell bodies (figure 4.6a). The difference likely reflects a higher surface-to-volume ratio in the dendritic compartment. Using Cal-590 and rapid two-photon scanning (500 Hz), we were able to resolve individual Ca^{2+} transients occurring during high-frequency trains (100 Hz) of action potentials (figure 4.6b). Considering the fast rise and decay times of the dye, an even better signal-to-noise ratio for the Ca^{2+} transients could be recorded with higher frame rates. Such recordings of the rapid kinetics of Cal-590 could be useful for the analysis of neurons with high action potential frequencies, such as L5 pyramidal neurons (Tischbirek *et al.*, 2015).
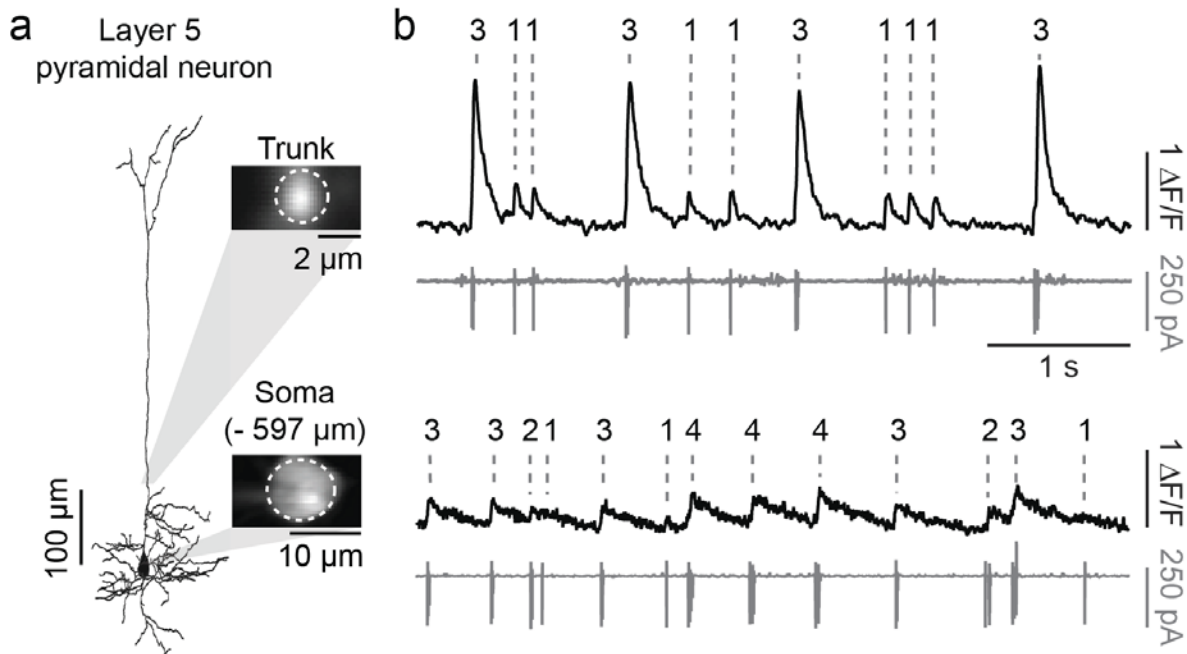
Figure 4.5: Imaging dendritic and somatic Ca^{2+} transients in individual neurons with Cal-590. Figure modified from Tischbirek et al., 2015

a. Reconstruction of the morphology of a L5 pyramidal neuron in the mouse visual cortex based on a z-stack projection recorded with two-photon imaging. The neuron was labeled in vivo by electroporation of Cal-590. Insets show the focal planes of the dendritic trunk and the soma (indicated by white dotted lines) at their respective recording depth. Note the electrode used for cell-attached measurements on top of the soma.

b. Black: Spontaneous Ca^{2+} transients recorded in the dendrite (top) and soma (bottom). Grey: Parallel somatic cell-attached recording showing action potentials. The number of action potentials (determined from the cell-attached recordings) is indicated on top of the Ca^{2+} transients.
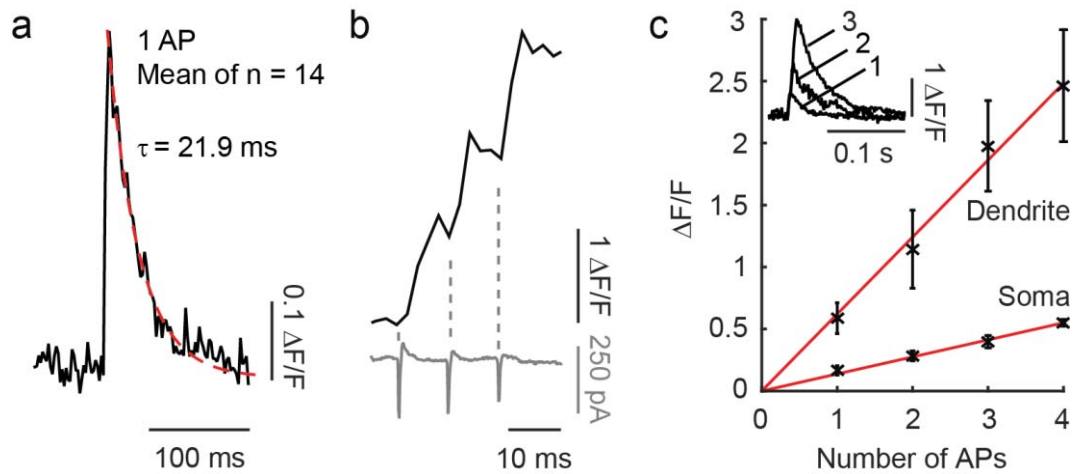
Figure 4.6: Kinetics of dendritic Ca^{2+} transients imaged with Cal-590. Figure modified from Tischbirek et al., 2015

a. Black: Dendritic Ca^{2+} transient recorded during single action potential events (mean of 14 events). Red dotted line: single exponential fit to determine the decay time constant. Imaging was performed at the same dendritic location as indicated in the previous figure.

b. Black trace: Ca^{2+} transient showing the rising phase of 3 consecutive action potentials (recorded at 500 frames/s in the dendritic location indicated in the previous figure). Bottom grey trace: cell-attached recording performed at the soma of the neuron in parallel.

c. Dendritic and somatic Ca^{2+} transient amplitudes shown for a different number of action potentials (mean ± s.d, red lines show linear fit.) Inset shows dendritic Ca^{2+} transients corresponding to one, two and three action potentials (traces are numbered accordingly).
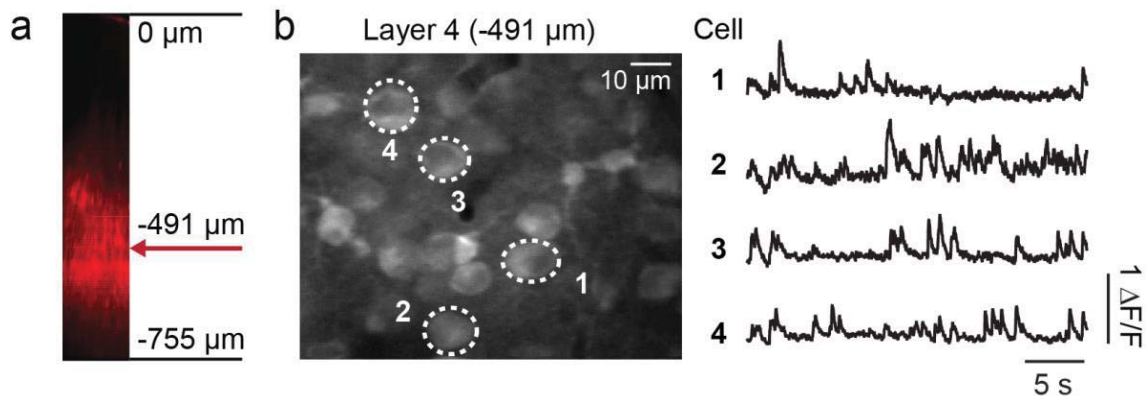
Figure 4.7: Two-photon Ca^{2+} imaging of neuronal populations in cortical layer 4 with Cal-590 AM. Figure modified from Tischbirek et al., 2015.

a. Side view of the z-stack recorded with two-photon imaging. L4 of the visual cortex was labeled with Cal-590 AM. Depths below the brain surface are indicated.

b. Left: Two-photon image of a local region in L4 (depth below the brain surface indicated with a red arrow in panel a) used for the recording of spontaneous Ca^{2+} transients. Ca^{2+} transients (right) correspond to the cells indicated in the image.

Another useful parameter of a Ca^{2+} indicator used for the analysis of neuronal activity is the linearity of the relationship between fluorescence amplitudes and the number of action potentials observed at the soma. When Ca^{2+} transient are recorded without electrophysiological validation, the linearity of the indicator allows a more accurate interpretation of the observed neuronal activity levels. For Cal-590, we recorded a linear relationship between the number of action-potentials and the corresponding Ca^{2+} transient amplitudes in the soma as well as in the dendrites (figure 4.6 c).

4.5 Ca^{2+} imaging of neuronal populations in deep cortical layers

To test Cal-590 AM for imaging neuronal activity in deep cortical layers with single cell resolution, we labeled a defined volume of cortical tissue in the desired imaging depths in layers 4 (figure 4.7), 5 and 6 (figure 4.8). Limiting the size of the stained region was important to limit out-of-focus fluorescence from regions overlying the focal plane (Birkner *et al.*, 2017). As the fluorescence of Cal-590 AM is not readily detectable in the injection pipette and immediately after ejection into the brain tissue, adding a spectrally separate fluorescence dye such as Alexa680 was crucial to label
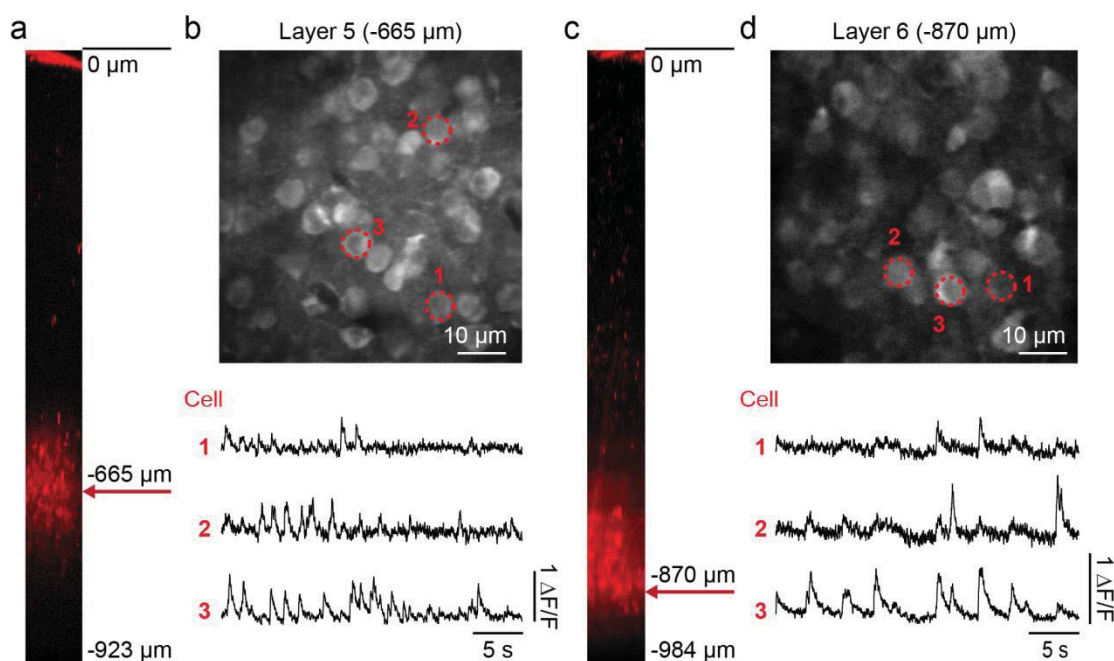
Figure 4.8: Kinetics of somatic Ca^{2+} transients imaged with Cal-590. Figure modified from Tischbirek et al., 2015.

a-b; Same panels as shown in the figure 4.7 above, but for a region in cortical layer 5.

c-d. Same as panels a-b, but for a region in cortical layer 6 stained with Cal-590.

defined volumes of tissue with diameters of about 200 µm (Tischbirek *et al.*, 2015). In the z-stack projections shown in figures 4.7 and 4.8, note the limited size of the stained regions, which labeled neurons in layer 4 (-491 µm), layer 5 (-665 µm) and layer 6 (-870 µm), respectively. In all depths, neuronal Ca^{2+} transients were observed. Especially the data from layer 5 and 6 showed recordings of neuronal activity in depths that were hardly accessible for two-photon imaging experiments before. To verify the sensitivity of the measurements in the deep layers, a region in a depth of 740 µm below the brain surface was stained with Cal-590. The combined cell-attached patch-clamp and two-photon Ca^{2+} imaging recording (figure 4.9) demonstrates the possibility to linearly detect very low numbers of action potentials even in very deep cortical regions.
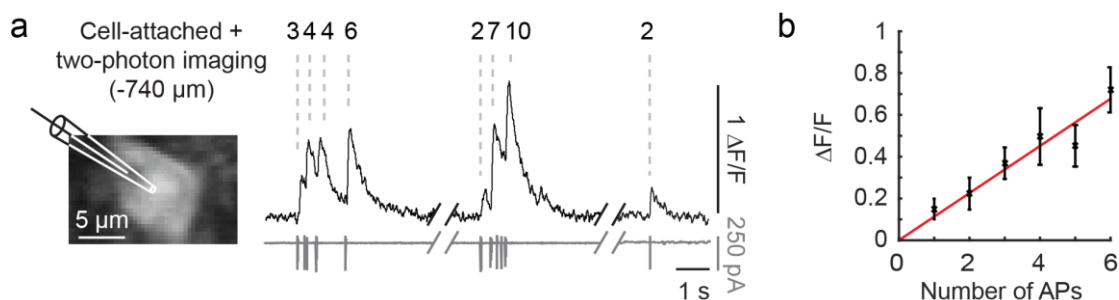

Figure 4.9: Imaging action potential-related somatic Ca^{2+} transients in deep cortical layers. Figure modified from Tischbirek et al., 2015.

a. Right: Neuronal soma recorded with two-photon imaging in cortical L5 (depth indicated above the image). Schematic of the cell-attached pipette is included to illustrate the recording configuration. Left: Ca^{2+} transients (black, top trace) and cell-attached traces (grey, bottom) recorded in parallel. Number of action potentials indicated above the Ca^{2+} transients.

b. Graph showing the linear fit (red line) of the number of action potentials and Ca^{2+} transient amplitudes as ΔF/F values (mean ± s.d.).

4.6   Dual-color Ca^{2+} imaging with Cal-590 and OGB-1

Because of the red-shifted emission spectra of Cal-590 compared to 'conventionally' used fluorescent Ca^{2+} indicator dyes such as OGB-1, we tested the possibility to perform simultaneous two-photon imaging experiment with both dyes. We labeled a population of neurons in layer 2/3 with Cal-590 AM and electroporated an individual neuron within the same population with OGB-1 (figure 4.19). When using the optimum excitation wavelength of Cal-590 AM around 1050 nm, OGB-1 is not excited efficiently and fluorescence cannot be detected from the individually OGB-1-labeled neuron. Similarly, with an excitation wavelength of 920 nm, no suseful signal can be recorded from the
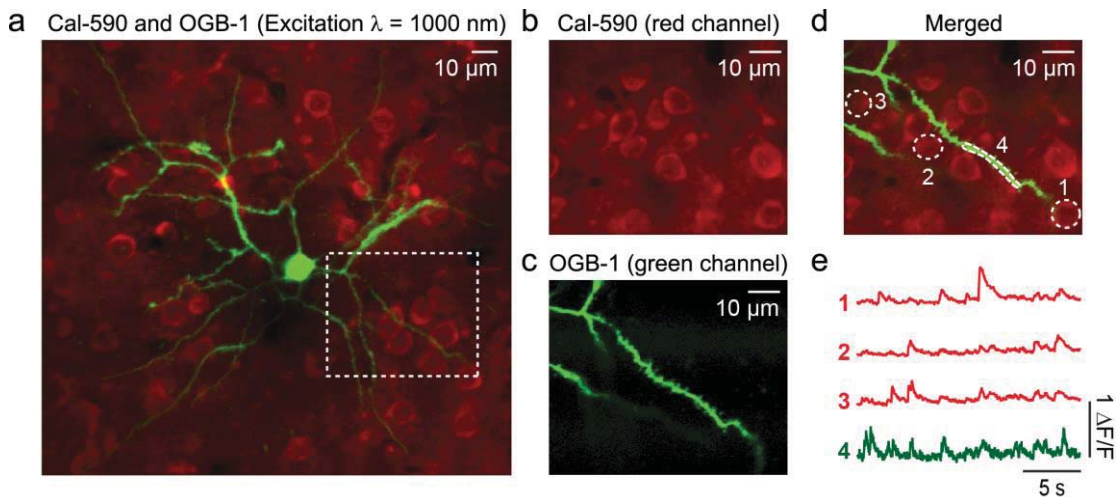

Figure 4.10: Dual-channel imaging of Ca^{2+} transients with Cal-590 AM and OGB-1 in vivo. Figure modified from Tischbirek et al., 2015.

a. Two-photon image of a population of neurons labeled with Cal-590 AM recorded simultaneously with a single neuron electroporated with OGB-1.

b.-c. Images show magnified recordings of the region indicated with the white dotted rectangular in panel a. In separate emission channels, Cal-590 (b) and OGB-1 (c) were recorded simultaneously.

d. Merged color channels of panels b-c.

e. Spontaneous Ca^{2+} transients recorded from Cal-590 labeled neurons (red channel). In parallel, Ca^{2+} transients were recorded from a dendritic segment of a neuron labeled with OGB-1 (green channel).

neurons stained with Cal-590. An option to record both dyes at the same time is the use of two excitation lasers, each tuned to the optimum wavelengths of both dyes. A second option is to use an intermediate excitation wavelength of 1000 nm. We used the second approach to reocrd Ca^{2+} transients with such an intermediate wavelength, and observed clear Ca^{2+} transients in both recording channels, which were separated by a dichroic mirror. We therefore demonstrated the potential use of Cal-590 in combination with another shorter-wavelength dye for dual-channel in vivo imaging experiments.

4.7 Sequential labeling with two spectrally separate Ca^{2+} indicators

For the purpose of creating a neuronal activity map of A1, we combined the two previously introduced techniques – flavoprotein autofluorescence imaging and deep two-photon imaging – for a sequential labeling approach: We identified the tonotopic gradient in the primary auditory cortex using autofluorescence imaging, and performed two-photon imaging in local fields of all cortical layers containing pyramidal neurons (L6, L5, L4 and L2/3). We began the sequence of local recordings with Cal-590 in layer 6. We started the two-photon imaging recordings in the deepest cortical layer (figure 4.11) to avoid out-of-focus fluorescence
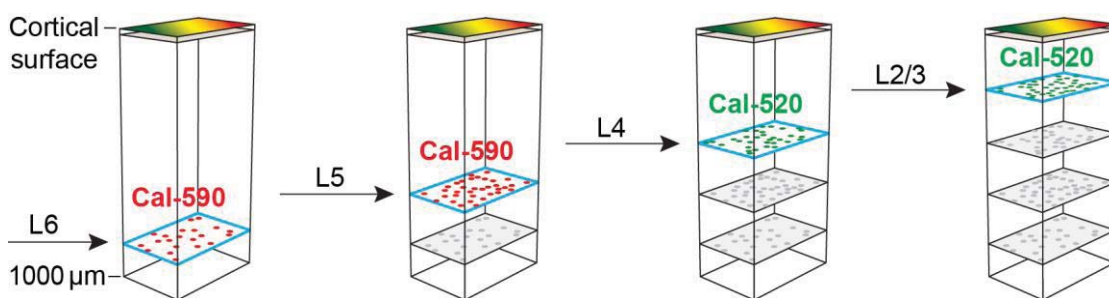

Figure 4.11: Sequential two-photon imaging of all cortical layers in a column-like structure with single-cell resolution

Illustration shows the sequence of staining and imaging steps for the measurement of neuronal activity in all cortical layers following the localization of A1 using flavoprotein autofluorescence imaging.

from overlying labeled brain tissue (Helmchen & Denk, 2005; Birkner *et al.*, 2017). After the tone-evoked responses in layer 6 were recorded, we repeated the staining and imaging steps in layer 5.

We observed that after recording in the deep cortical layers, Cal-590 diffused into the apical dendrites of layer 5 and layer 6 neurons. The
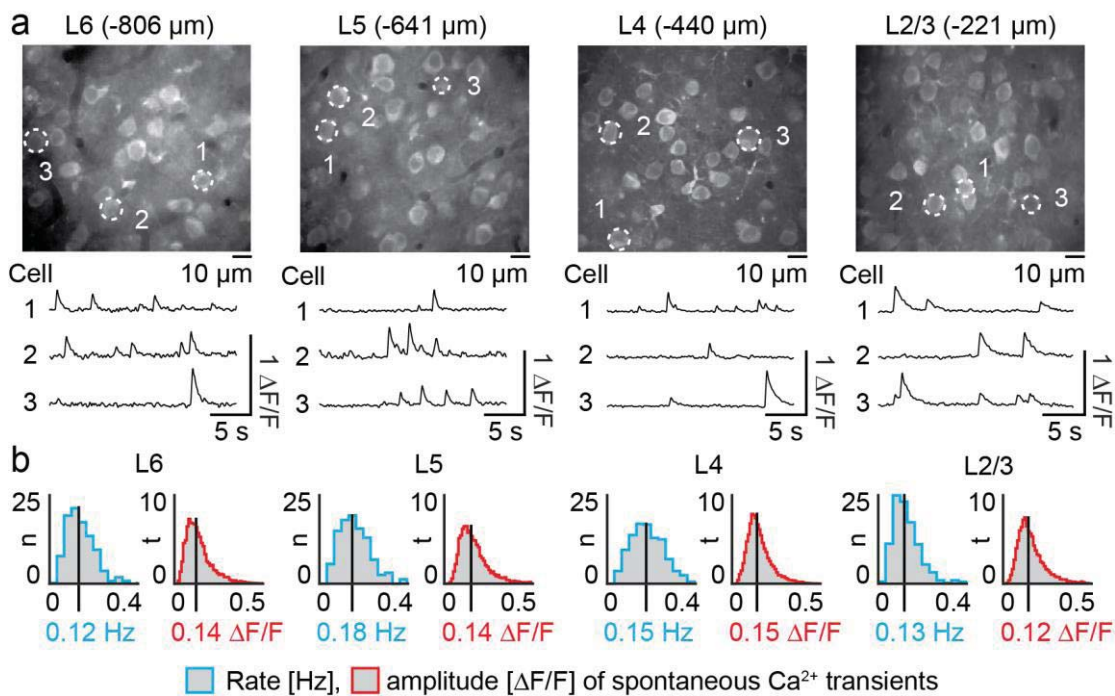
**Figure 4.12: Analysis of spontaneous neuronal activity in all cortical layers**

a. Two-photon imaging of cortical neurons using Cal-590 AM as a fluorescence indicator. Top: Example regions from layer 2/3, 4, 5 and 6 (from left to tight) in A1 are shown. The recording depth from the brain surface is shown above the images (average of 2,480 frames at 80 Hz). Bottom: Representative spontaneous Ca^{2+} transients. Numbers correspond to neurons indicated by white dotted lines in the top panels.

b. Histograms of the rate of spontaneous Ca^{2+} transients (blue) and corresponding ΔF/F values (red) for all layers in A1. Black vertical line marks the median value indicated below the histogram. n = % of cells. Absolute cell number: L2/3 = 385, L4 = 161, L5 = 502, L6 = 496. t = % of transients. Absolute transient number: L2/3 = 7014, L4 = 6347, L5 = 15304, L6 = 8439.

diffusion in turn caused increased background fluorescence in the upper cortical layers, reducing the signal quality of any additional labeled regions with Cal-590 in layers 4 and 2/3. To avoid this problem, we switched to the spectrally separate Ca^{2+} dye Cal-520 AM (Tada *et al.*, 2014). We stained layer 4 with Cal-520 AM and recorded Ca^{2+} transients without signal contamination from the dendrites originating in the lower cortical layers. In a final step, we repeated the procedure in layer 2/3 (L2/3, figure 4.11).

We analyzed the spontaneous neuronal activity recorded in all layers in the absence of auditory stimulation. For layer 5, we found a higher rate of spontaneous Ca^{2+} transients compared to the other cortical layers (figure 4.12, Kruskal-Wallis test, $\chi^2 = 164$, $p = 2.3 \times 10^{-35}$; Mann-Whitney U test between layer 5 and the other layers with Bonferroni–Holm correction, $p < 0.01$), which fit well to previous multiunit electrode recordings (Christianson *et al.*, 2011). Additionally, we found comparable amplitude distributions of spontaneous Ca^{2+} transients throughout all cortical depths, indicating a consistent recording quality for all layers.

As a control experiment, we tested for differences of the neuronal Ca^{2+} transients reported with both Cal-590 AM and Cal-520 AM. In separate samples, regions were labeled with one of the dyes. Spontaneous Ca^{2+} transients recorded for both samples. Importantly, we found no significant difference for the rate of spontaneous Ca^{2+} transients in layer 2/3 with both dyes under the recording conditions used here (Mann-Whitney U test, $p = 0.26$, figure 4.13). It should be noted though that Cal-520 showed a dye better retention in the sample neurons compared to Cal-590, and allowed for longer recording durations. Taken together, the sequential procedure made it possible to localize the primary auditory cortex and analyze neuronal activity in a column-like structure spanning the entire depth of the cortex. The unique advantage of our approach is the possibility to record from all layers within one animal at the same cortical location.
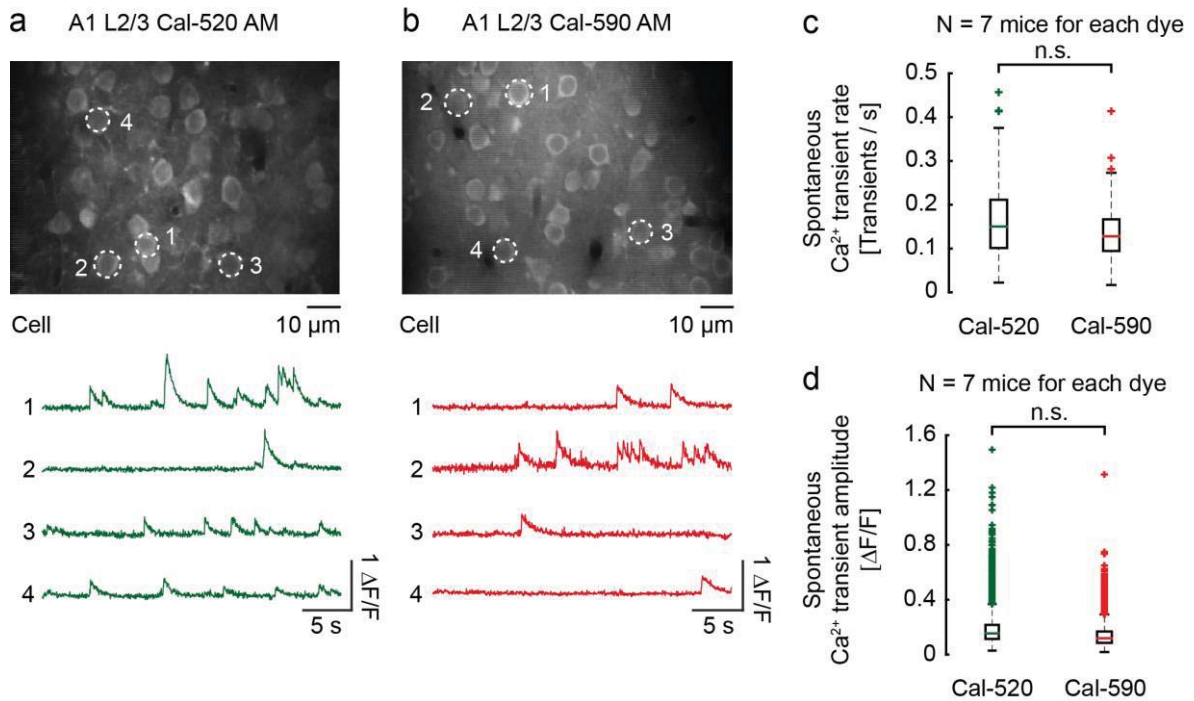
Figure 4.13: Comparison of Ca^{2+} transients recorded with Cal-520 AM and Cal-590 AM in cortical layer 2/3

a. Upper panel: Example image of cortical L2/3 labeled with Cal-520 AM (average of 2480 frames recorded at 80 Hz). Regions of interested indicated with white dotted circles. Lower panel: Representative spontaneous neuronal Ca^{2+} transients recorded in regions of interest 1-4 indicated in the upper panel.

b. As panel a, with cortical L2/3 labeled with Cal-590 AM.

c. Spontaneous Ca^{2+} transient rate of L2/3 neurons labeled with Cal-520 AM or Cal-590 AM (no significant difference, Mann-Whitney U test, p = 0.259, n = 7 mice for each group).

d. Spontaneous Ca^{2+}-transient amplitudes of the recordings shown panel c. Under the recording conditions used here, transients from neurons labeled with Cal-520 AM were not significantly different from Cal-590 AM (Mann-Whitney U test, p = 0.0530). However, note the tendency for larger signal amplitudes with Cal-520 AM.

4.8 Sound-evoked Ca²⁺ transients in all cortical layers

For an analysis of sound-evoked activity at the single-cell level, we recorded neuronal responses to up to 950 pure tones with 19 different tone frequencies (2-45.3 kHz equally spaced on a logarithmic axis) at 5 attenuation levels ranging from 20 to 70 dB SPL. Each stimulation condition was presented 8-10 times (Rothschild *et al.*, 2010; Chen *et al.*,
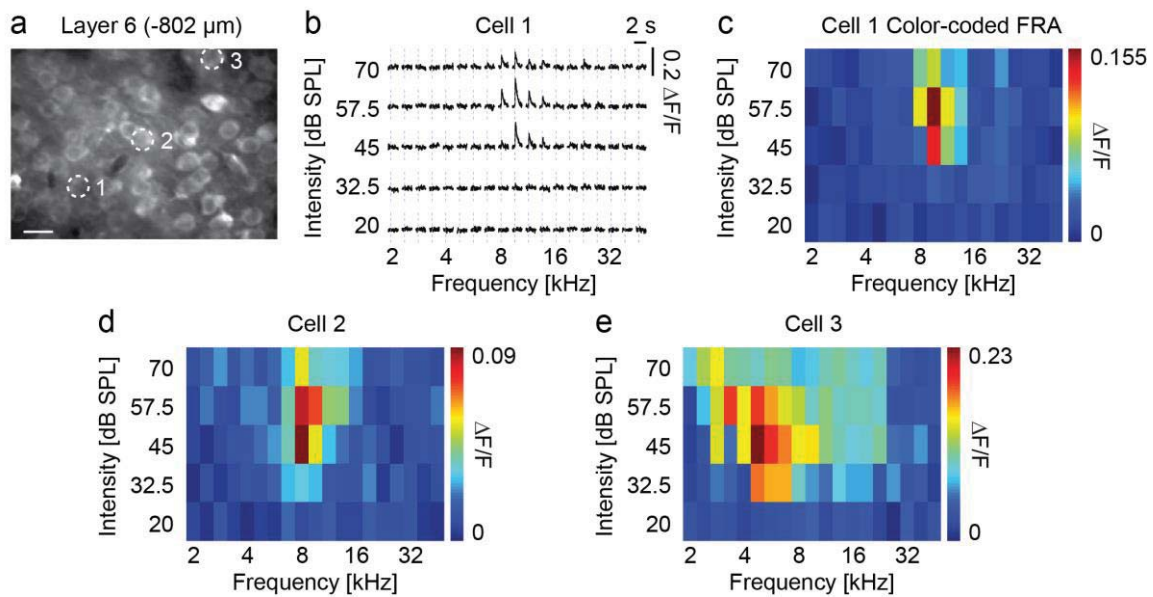
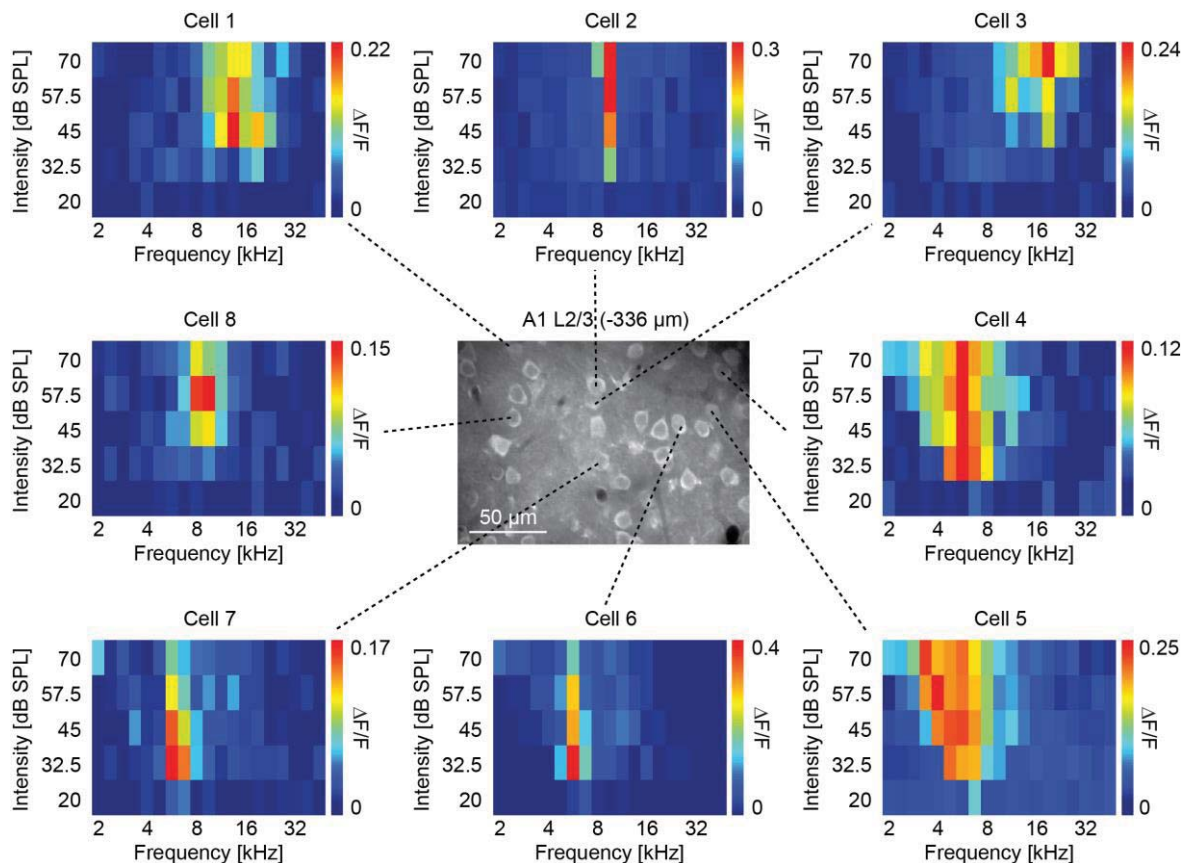**Figure 4.14: Frequency response areas describe the response of individual neurons to pure tone stimulation**

a. Two-photon average image of neurons in L6 of A1. White dotted line indicates region of interest of exemplary cell 1. Scale bar: 10 µm.

b. Average Ca²⁺ transient amplitudes for all frequency-intensity combinations of an example neuron are displayed as the cell's frequency response area (FRA). The FRA shown here reveals that cell 1 of panel a. was responsive to pure tone stimulation and most responsive to frequencies around 9.5 kHz.

c. FRA color-coded according to the average Ca²⁺-transient amplitude for example cell 1 indicated in a.

d-e. FRAs of two different example cells indicated in panel a. Note the diversity of FRAs.

2011). We observed tone-evoked Ca^{2+} transients for each neuron identified in two-photon imaging planes (see figure 4.14 for an example recording in layer 6), with variable frequency responses within local imaging fields (example from layer 2/3 shown in figure 4.15). Regarding the stimulation parameters chosen to record the tone-evoked responses, it was desirable to have as many stimulation conditions as possible for a detailed analysis of the frequency- and intensity-dependent functional properties of individual neurons. However, the overall recording duration increases with each additional stimulation condition. Thus, the stimulation parameters were chosen to balance the resolution of the frequency


Figure 4.15: Diversity of neuronal frequency-response areas in A1
An example two-photon image of a local region in A1 layer 2/3 is shown in the center. The FRAs of individual neurons are arranged in the surrounding panels. Note the difference of individual FRAs. Black dotted lines point to the location of cells 1-8.

response area (FRA, which is the matrix summarizing the response of an individual neuron to each individual stimulation condition), and the recording duration for a single field-of-view. The separation between stimulation frequencies was 0.25 octaves, in line with the relatively wide tuning of neurons in the mouse auditory cortex (Linden *et al.*, 2003; Guo *et al.*, 2012). Individual stimuli were followed by a 1.5 s break, which allowed for the decay of stimulation-induced Ca^{2+} transients, but at the same time allowed for a reasonable recording duration for all 950 stimuli.

Using these stimulation parameters, we recorded sound-evoked Ca^{2+} transients for each neuron identified in all layers of the primary auditory cortex. A similar percentage of neurons (69.9 ± 6.74 %, Pearson's χ^2 test, $\chi^2 = 78.0$, p = 0.294, figure 4.16) responded to pure tone stimulation in all cortical layers. Responses shown in figure 4.16 are divided into neurons, which were frequency-tuned with preferential responses to certain tone frequencies, responsive neurons without such frequency-specific responses, and neurons showing spontaneous Ca^{2+} transients, but no tone-evoked responses.
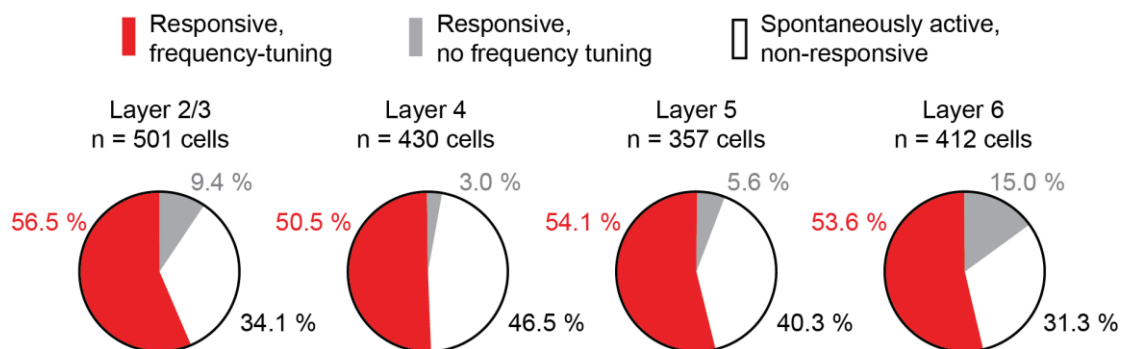
Figure 4.16: Percentage of neurons responsive to pure tone stimulation

Percentage of neurons responding to pure-tone stimulation in each layer of the primary auditory cortex (categories are described in detail in the Methods section, dataset n = L2/3 = 11, L4 = 12, L5 = 9, L6 = 14 animals).
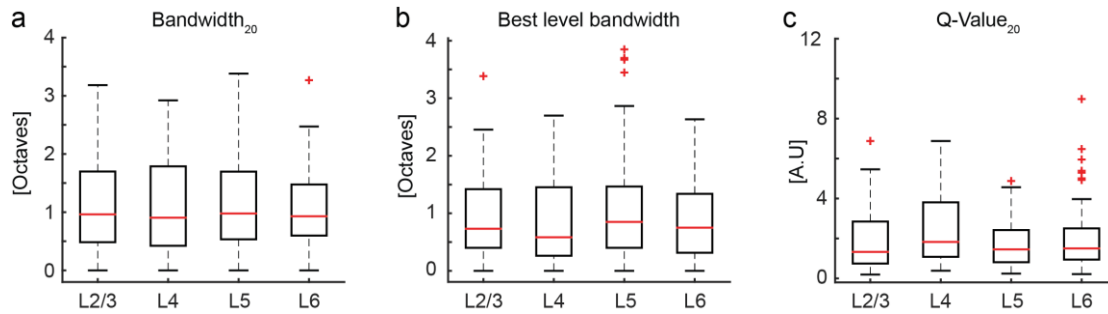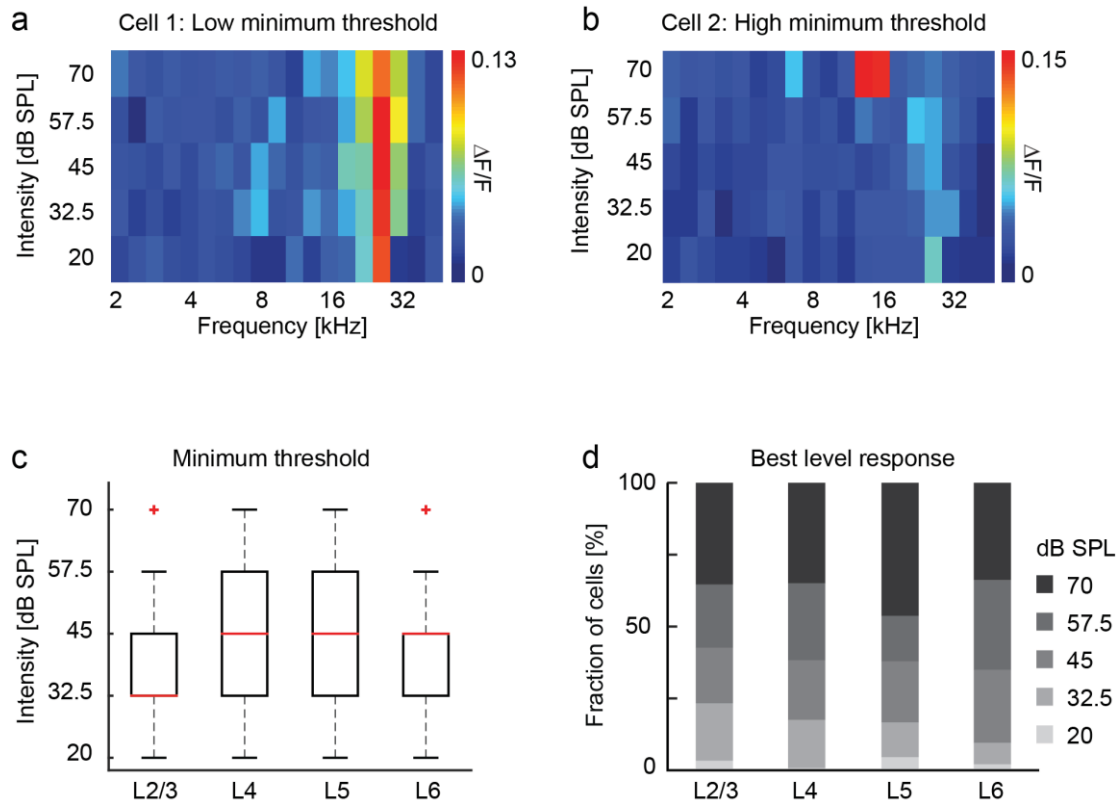
Figure 4.17: Tuning properties of neurons in each layer of A1: Tuning width

a. Plot showing the tuning bandwidth at 20 dB above minimum threshold of neurons in each cortical layer. Kruskal-Wallis test, χ^2 = 0.46, p = 0.927, no significant difference between the individual layers was observed.

b. Plot showing the bandwidth at the best sound level of neurons in each cortical layer. Kruskal-Wallis test, χ^2 = 1.74, p = 0.628, no significant difference between layers was observed.

c. Plot showing the Q-value$_{20}$ (BF/bandwidth$_{20}$) of neurons in each cortical layer. Kruskal-Wallis test, χ^2 = 4.49, p= 0.214, no significant difference between layers was observed.

Next, we analyzed the corresponding FRAs, and determined various parameters describing the properties of frequency-tuned neurons in all layers. As shown in figure 4.15, we observed very diverse frequency responses in local fields, and the parameters included in the analysis were chosen to describe differences of the tuning width (figure 4.17), intensity threshold and best level response (figure 4.18). For none of the parameters we found a significant difference between individual layers. Thus, FRA parameters of individual neurons were remarkably similar in all layers of the cortex. As a control for the quality of the recorded FRAs through the different layers, we calculated the d' value (see methods), which had a comparable signal quality in all cortical layers (median of d' distribution > 8.89 for all layers).

Figure 4.18: Tuning properties of neurons in each layer of A1: Minimum threshold

a. Example FRA of a neuron responding to pure tones at 26.9 kHz. Note the similar Ca^{2+} transient amplitudes regardless of the sound intensity (20 to 70 dB SPL).

b. Compared to panel a, the neuron has a higher minimum threshold and only responds to pure tone stimulation at 70 dB SPL.

c. Box plots of the minimum threshold in all cortical layers. No significant difference was observed for the individual layers (Kruskal-Wallis test, χ^2 = 5.45, p = 0.142).

d. Bar graphs showing the fractions of best level responses in all cortical layers. Pearson's χ^2 test, χ^2 = 620.0, p = 0.359, no significant difference between the fractions of the different cortical layers.

4.9   Limited local heterogeneity of best frequency responses

We next analyzed the best frequency (BF) responses of individual neurons. The BF describes the stimulation frequencies which evoked the largest mean Ca^{2+} response in individual neurons and is an important parameter to describe their frequency-tuning properties (Rothschild *et al.*, 2010). Importantly, BF responses were virtually unchanged in awake animals and lightly anesthetized animals (figures 4.19), in line with previously shown results (Li *et al.*, 2017), with a very similar BF IQR value for both conditions (figure 4.20). Thus we were able to use stable, consistent recording conditions with anesthetized animals for our experiments.
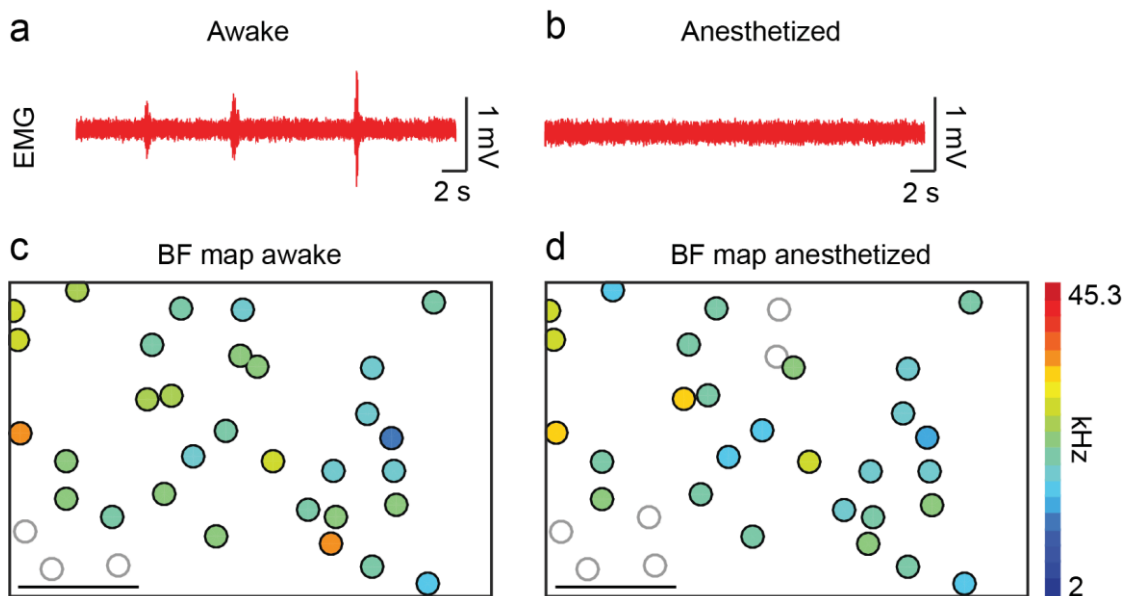
Figure 4.19: Difference of BF responses in awake and anesthetized animals

a. EMG recording showing high-frequency bursts during wakefulness.

b. During MMF anesthesia, the EMG recording from the same animal as in panel a showed no high-frequency activity.

c. BF map. Individual neurons are indicated by symbols color-coded according to their BF. Empty circles show neurons without frequency tuning. Scale bar = 50 µm.

d. Same as in c, but recorded during an anesthetized state of the animal. Note the slightly lower number of tuned cells in this example recording.
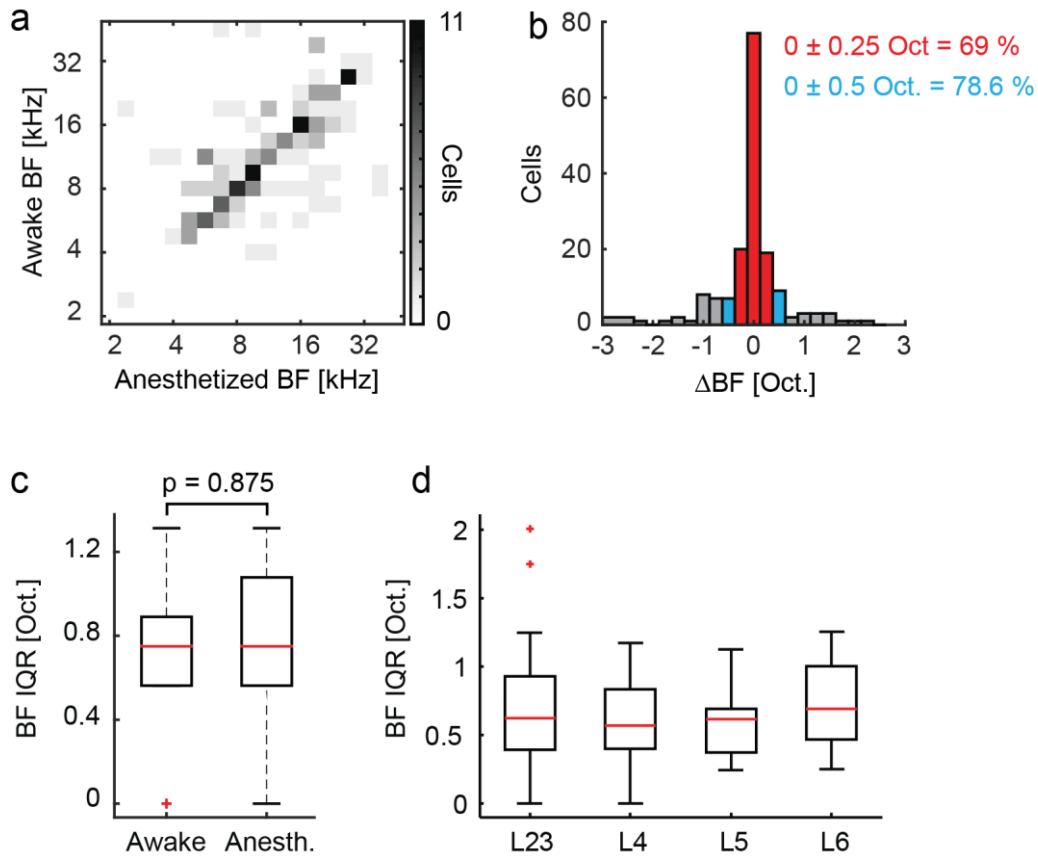
Figure 4.20: Comparing BF responses during awake and anesthetized recording conditions

a. Correlation of BF responses during wakefulness and anesthesia in n = 5 animals (Pearson's correlation coefficient R = 0.668, p = 4.83 × 10^{-23}). Individual data points are intensity-coded according to the scale on the right side of the graph.

b. Histogram of the BF difference (ΔBF) of individual cells under wake and anesthetized recording conditions. The percentages of all recorded neurons, which had a ΔBF value of ± 0.25 and 0.5 octaves, are indicated in red and blue, respectively.

c. Box plot showing the BF variability (interquartile range: IQR) during wakefulness and anesthesia (Wilcoxon signed-rank test p = 0.875).

d. Plot showing the BF IQR in anesthetized animals for each cortical layer. Values are based on the same fixed analysis window size in all layers (200 x 130 μm). No significant difference was found between the individual layers (Kruskal-Wallis test, χ^2 = 0.73, p = 0.865).

While awake recordings are generally desirable for sensory stimulation experiments to exclude effects of the anesthesia on neuronal activity patterns, the awake-like conditions we developed here allowed long recording durations, avoided unnecessary tension conscious animals might experience during the stimulation paradigm with loud tones, and a safe re-insertion of the labeling pipettes into non-moving brain tissue following imaging session of each individual layer.

4.10 Limited local heterogeneity of best frequency responses

Ca^{2+} transients corresponding to the BF of example neurons recorded in all layers at the same cortical location in one example mouse are shown in figure 4.21. In a local field of view, the BF responses of neighboring neurons were variable despite their spatial proximity (figure 4.21b). However, the variability did not range across all stimulation frequencies presented to the mouse (figure 4.21c). Instead, it was limited to a narrow range of the stimulation frequencies. The degree of variability was similar in all cortical layers (Bartlett's statistic for difference of variability between layers = 4.65, p = 0.199).

For an analysis window of 200 x 130 μm, we found a variability of R_{90} = 1.55 ± 0.13 octaves (figure 4.22, average for all layers, n for each layer: L2/3 = 26, L4 = 18, L5 = 15, L6 = 18 animals). For a different method to calculate the heterogeneity see figure 4.20d, which shows a similar BF IQR value in all layers. The narrow-band BF variability reported here was lower than the variability reported for the first two-photon imaging recordings in layer 2/3 of the auditory cortex (Bandyopadhyay *et al.*, 2010; Rothschild *et al.*, 2010; Winkowski & Kanold, 2013). However, the value reported here was substantially larger than observed with the genetically-encoded Ca^{2+} indicator GCaMP3 (Issa *et al.*, 2014), and the value recorded for layer 4 (Winkowski & Kanold, 2013). Thus, we observed an intermediate BF variability in relation to results previously published for the upper cortical layers, and show that the BF variability is consistent throughout the entire cortical depth.
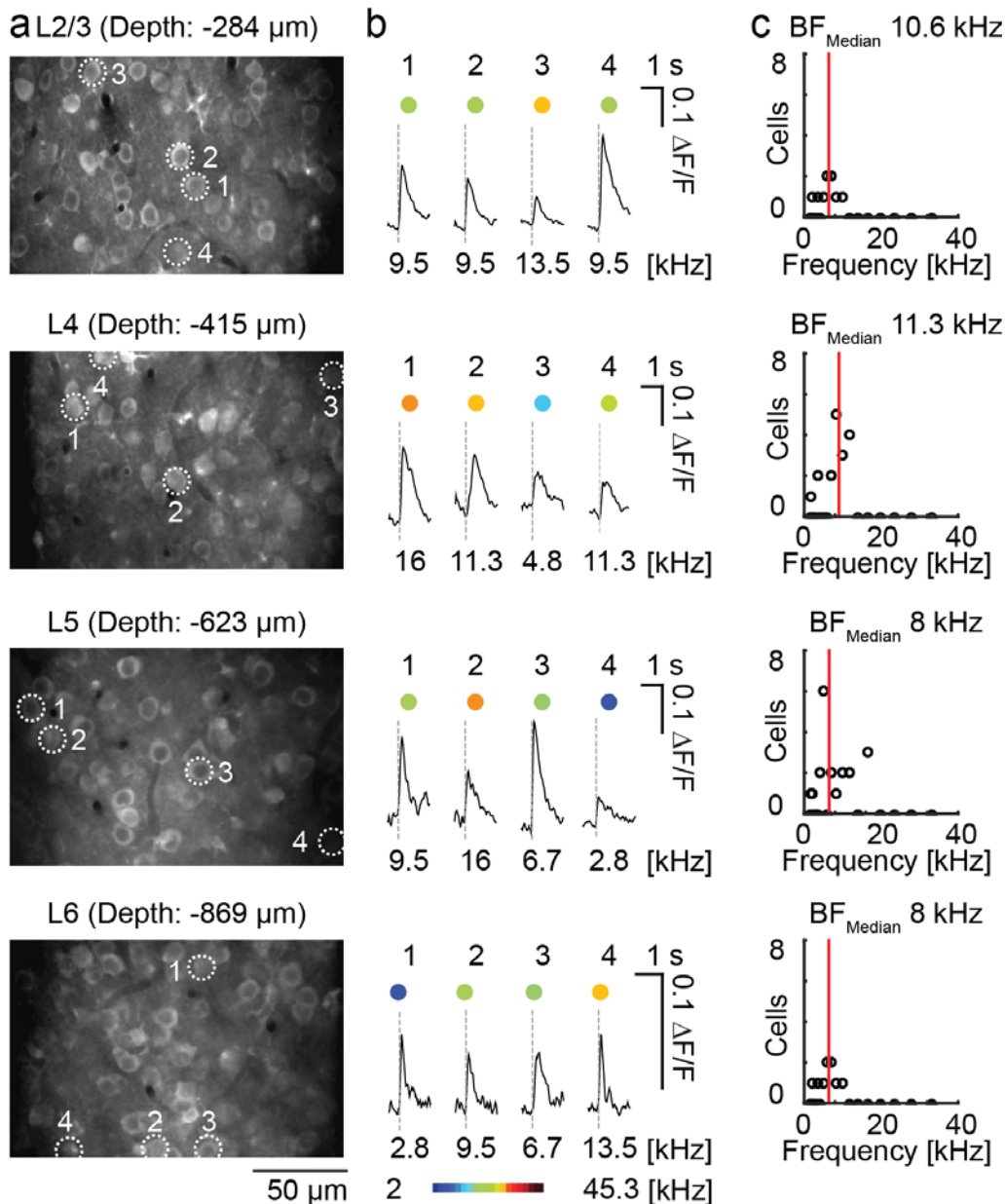
Figure 4.21: The local heterogeneity of best frequency (BF) responses is limited

a. Example two-photon images of all cortical layers in A1. Layers and recording depth is indicated above the image.

b. For individual neurons indicated in panels a, the representative sound-evoked Ca^{2+} transients of the BF response is shown (average of 7-10 trials). The tone frequency eliciting the BF response is indicated below the transient and by the colored symbols.

c. For the example images shown in panel a, histograms of the BFs observed within the field of view are shown. The red line indicates the median value, which is also noted above the histograms (BF$_{median}$).
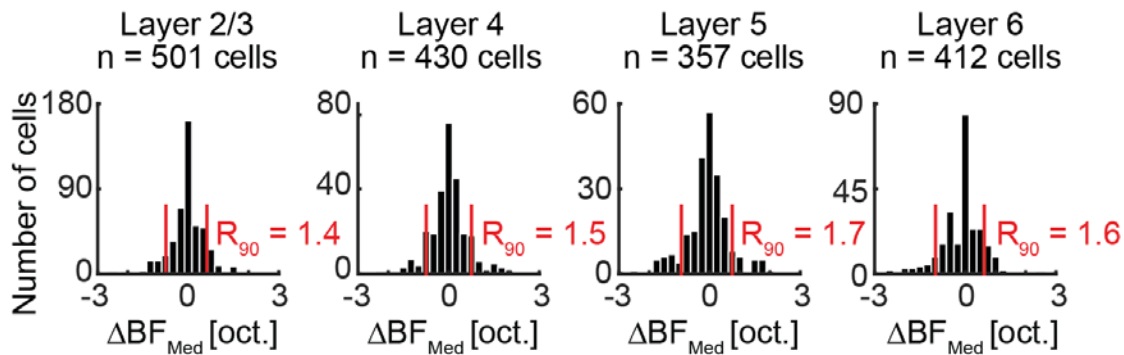
Figure 4.22: Limited heterogeneity in local fields

For all cortical layers, the difference of the BF of individual neurons from the median BF of the respective imaging field is shown. The R_{90} value in octaves (90% range of the histogram) is indicated by vertical red lines and noted in the histograms.

4.11 Preserved large-scale tonotopy in primary auditory cortex

We next examined the relationship between the local BF heterogeneity and the tonotopy observed at the cortical surface. From a recording showing multiple neighboring field-of-views in layer 2/3 (figure 4.23), it becomes immediately apparent that the tonotopy of BF responses is preserved on the level of individual neurons despite the local heterogeneity. On the left side of the image, corresponding to the anterior/rostral section of auditory cortex, higher frequency responses are shown in red. On the right side of the image (posterior/caudal), lower frequency responses are shown in blue. In total, a distance of approximately 750 μm along the tonotopic axis is shown. The observation fits to the previously observed tonotopic organization in layer 2/3 (Rothschild *et al.*, 2010; Issa *et al.*, 2014).
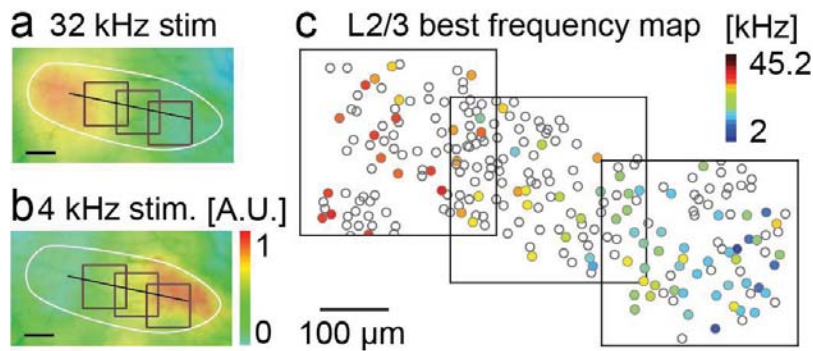
Figure 4.23: BF responses of individual neurons along the brain surface gradient

a. Flavoprotein autofluorescence images during tone stimulation with 32 kHz and b. 4 kHz. Black line indicates the tonotopic axis of A1 (estimated A1 borders indicated by white line). Scale bars: 200 μm.

c. Example recording of 3 adjacent imaging sites in cortical layer 2/3 of A1. The imaging region is indicated by the black rectangles in panels a-b. Individual neurons are shown as symbols color-coded according to their BF (color scale shown on the top right). Neurons without frequency tuning are marked by empty circles.

Our recordings from all cortical layers revealed that the organizational pattern extends through the entire depth of the primary auditory cortex. As shown for example regions from all cortical layers, neurons with higher best frequencies are located in more rostral regions, and neurons with lower best frequencies are located in more caudal regions (figure 4.23a). A comparison of median best frequencies of a local region observed with two-photon imaging with the BF extrapolated from the autofluorescence imaging data showed a strong correlation between both recordings (figure 4.23b, Pearson's correlation coefficient R in each layer L2/3 = 0.89, L4 = 0.89, L5= 0.60, L6 = 0.61, $p < 0.05$ in all layers, n for each layer: L2/3 = 26, L4 = 19, L5= 14, L6 = 16 animals). Thus, we show that the brain surface tonotopic gradient is preserved at the level of individual neurons in all layers of the cortex.
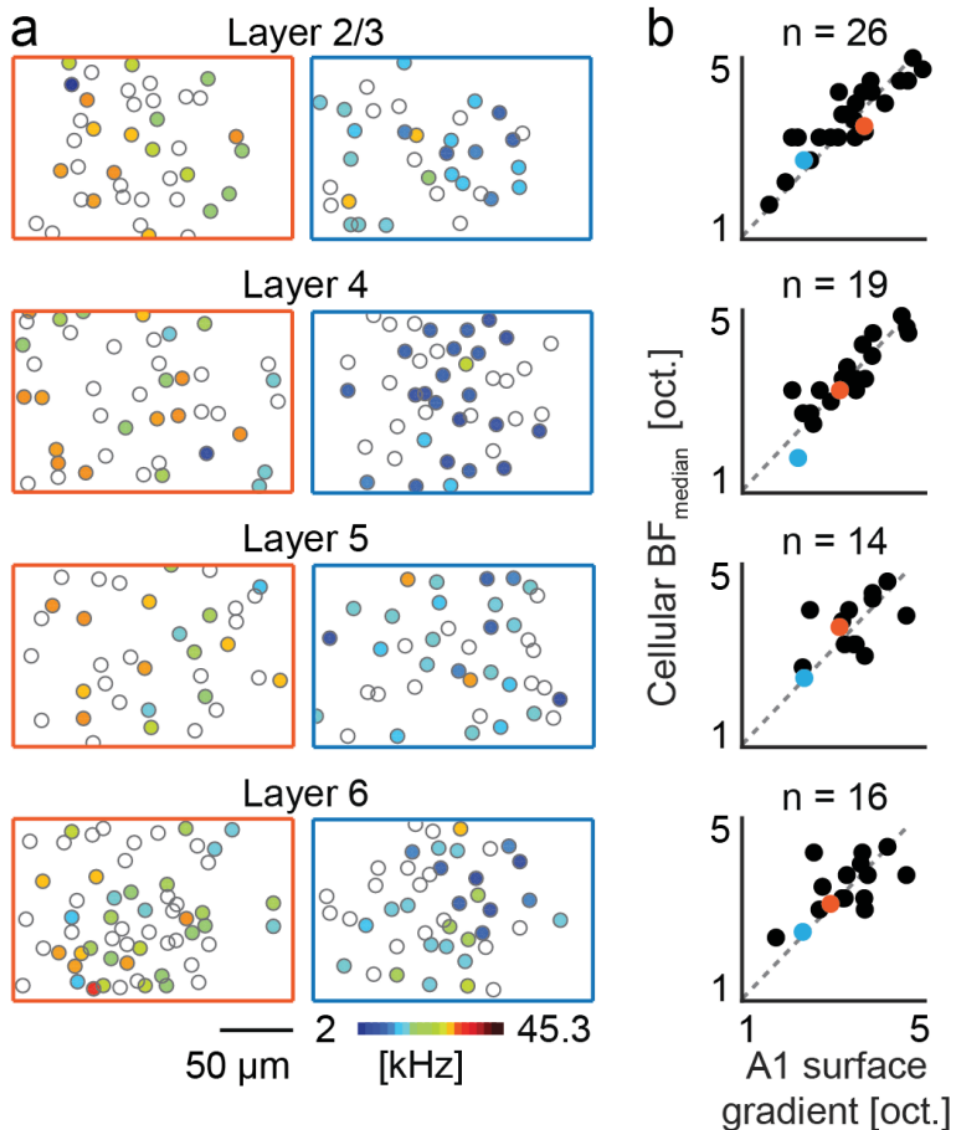
Figure 4.24: Local BF responses are preserved throughout all cortical layers and along the brain surface gradient

a. For each layer, a BF map of a higher (orange frame) and lower (blue frame) frequency region is shown.

b. Correlation of cellular BF$_{median}$ values recorded with two-photon imaging and the corresponding brain surface frequencies extrapolated from flavoprotein autofluorescence imaging. The regions shown in panel a are marked by orange and blue symbols.

4.12 Cellular organization of best frequency responses

Does auditory cortex consist of functional columns? Such columns have been reported for other cortical regions (Mountcastle *et al.*, 1955; Hubel & Wiesel, 1968), and have long been suggested to also exist in auditory cortex (Oonishi & Katsuki, 1965; Abeles & Goldstein, 1970; Merzenich *et al.*, 1975). However, the analysis of a columnar organization with single-cell resolution in the primary auditory cortex has not been done before.

Because of the lateral location of the primary auditory cortex in the mouse brain (compare figure 4.2), it is situated in an area with pronounced brain curvature. As a consequence, the accurate alignment of different cortical layers is difficult. We used the apical dendrites of layer 5 pyramidal neurons, which are arranged perpendicular to the cortical surface, as markers for the columnar axis. In individual experiments, we labeled up to 20 layer 5 pyramidal neurons by single-cell electroporation of A680 (figure 4.25a) just before Ca^{2+} imaging in the upper cortical layers. The labeled dendrites were used as guides to align layer 2/3 and 4 with the corresponding regions of layer 5, and by extension of the dendritic axis to layer 6. A posthoc analysis of two-photon z-stack projections allowed the precise alignment of imaging regions.

In a column-like bundle of layer 5 apical dendrites, neurons with higher best frequencies (marked in red) tended to cluster on the right edge of the imaging field while those with lower best frequencies (marked in green and blue) were more abundant on the left edge (figure 4.25b). On average, the neurons were arranged along a significant tonotopic gradient in all cortical layers, even at a distance as short as 100 μm (figure 4.25c, linear regression $p < 0.05$ for each layer; see figure 4.27a-h for representative example experiments). The gradients were similarly steep in all layers (figure 4.25c), and were not significant along the transverse orientation (figure 4.26). On average, the direction of the gradients observed at the cellular scale had the same direction as the brain surface tonotopic gradient observed with autofluorescence imaging (figure 4.27i).
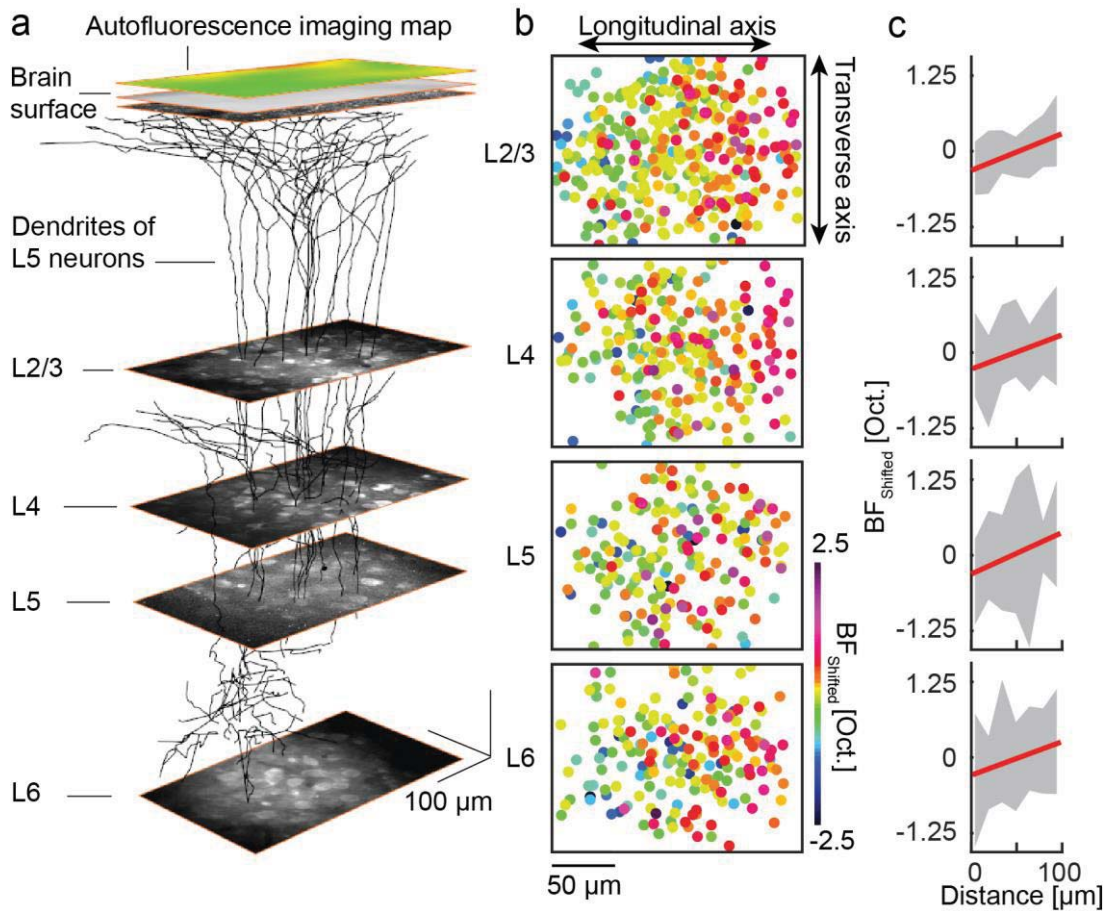
**Figure 4.25: Cellular organization of the primary auditory cortex**

a. Reconstructed imaging region showing flavoprotein brain surface image, two-photon imaging planes of L2/3 to L6 and dendrites of L5 pyramidal neurons.

b. BF maps of L2/3 to L6. Overlay of multiple experiments (n for each layer: L2/3 = 20, L4 = 17, L5 = 13, L6 = 11 animals). Each neuron is indicated by a circle colored according to its BF (difference from BF_{median} is used to align multiple experiments). The color scale is shown on the bottom right. Images from multiple experiments were overlaid according to their longitudinal axis, along which the maximum BF gradient was observed in each experiment.

c. Linear regression showing the BF gradient for a distance of 100 μm along the tonotopic axis of A1 ($p < 0.05$ along the longitudinal axis for each layer). The standard deviation is indicated by grey shades (bin size 15 μm).

Along the gradient, the separation of neurons with similar best frequencies was not abrupt, and distances between neurons with the same BF could exceed 400 µm (average R_{90} value for 2-5 octaves = 419.3 µm, figure 4.29). Previous studies have not reported BF gradients along such a short distance (Bandyopadhyay *et al.*, 2010; Rothschild *et al.*, 2010; Winkowski & Kanold, 2013)

Considering the BF gradient observed at short distances around 100µm, we wondered about the minimum distance at which the BF change becomes significant. To measure the minimum distance along the tonotopic axis necessary for a significant BF change, we applied two rectangular analysis windows (width 30-90 µm, length 130 µm) to a local imaging region. The distance between the two analysis windows was systematically increased. To illustrate the results, figure 4.28 shows an example region from layer 6 with significantly different best frequencies at a distance of 100 µm (Mann Whitney U-test, p-values after
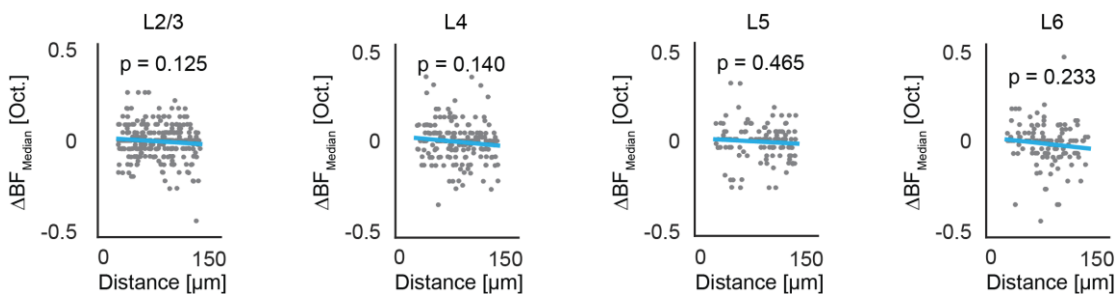
Figure 4.26: BF gradients along the isotonotopic axis orthogonal to the brain surface tonotopic gradient

Graphs showing the BFs of individual cells (grey symbols) along the axis orthogonal to the brain surface tonotopic axis. Data for L2/3 to L6 is shown from left to right. DBF$_{Median}$ is used to offset absolute frequency differences between individual recordings to pool multiple experiments (n for each layer: L2/3 = 20, L4 = 17, L5 = 9, L6 = 8 animals). Blue lines show the linear regression of the BF distributions (p > 0.05 in L2/3 to L6).
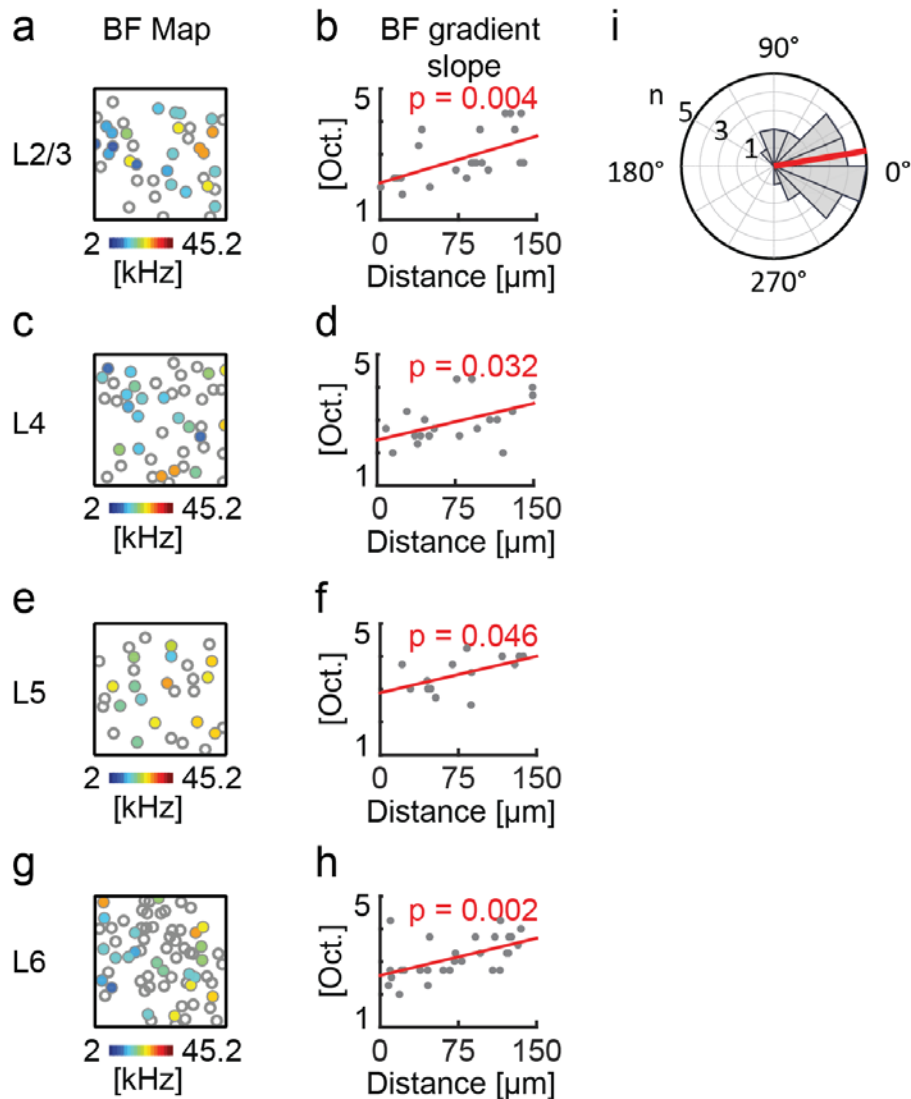
Figure 4.27: Tonotopic gradients on the cellular level

a. Example analysis window (sized 150 µm x 150 µm) of a two-photon imaging region in A1 L2/3. Individual cells are colored according to their BF. Empty symbols show neurons without frequency-tuning.

b. For the data shown in panel a, BF along micro-tonotopic axis (see Methods) in panel a. Each grey dot is one tone-responsive cell. Linear regression line and significance level shown in red.

c-h. Same as panel a-b for example regions in layers 4, 5 and 6 of A1.

i. Circular histogram showing the angular difference between the tonotopic axes based on either local cellular gradients (two-photon imaging of individual neurons) or brain surface gradients (flavoprotein autofluorescence imaging). Red line: median angle (n = 27 animals). No significant difference between the two axes was observed (circular statistical test for median angle from 0°, p = 0.70).
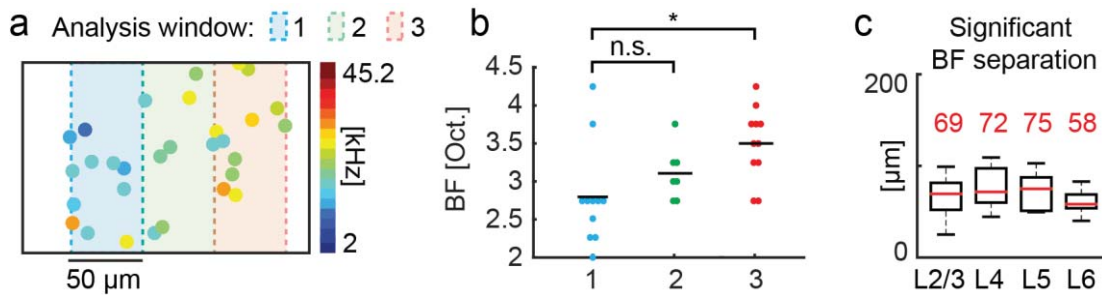
Figure 4.28: Distinct frequency bands encompassing all cortical layers of A1

a. Example L6 region with neurons color-coded according to their BFs. Three analysis windows (50 x 130 µm) are indicated in blue, green and red.

*b. Plot showing BFs of neurons inside the analysis windows indicated in panel a (symbols are colored according to the respective analysis window). Median BF of each analysis window shown as a black line. P-value significance indicated above the graph (Mann-Whitney U test with Holm-Bonferroni method, p < 0.05 = *; exact values in text).*

c. Analysis of the distance along the tonotopic axis necessary to reach a significant BF change. The red numbers indicate the median distance for a significant BF change in µm for each layer.

Bonferroni-Holm correction: 1 vs 2: 0.124.; 1 vs 3: 0.0396; 2 vs 3: 0.103). In more detail, figure 4.30 shows for an example region how the difference of the BFs observed in the two windows increased according to the distance between them until it reaches a significance at p = 0.05. In each cortical layer, the shortest distances necessary to reach significant differences (L2/3 = 69 µm, n= 20; L4 = 72 µm, n = 17; L5 = 75 µm, n = 13; L6 = 58 µm, n = 11 experiments) were quite similar to each other (figure 4.28c, Kruskal-Wallis test for difference between layers: χ^2 = 2.79, p = 0.425).

In conclusion, we have not observed functional columns separated by sharp frequency steps in the primary auditory cortex. Instead, we find smoothly overlapping columns, which can be described as 'sliding' along the tonotopic axis of the auditory cortex, as they preserve their functional

properties without a fixed midpoint at defined positions along the tonotopic axis.
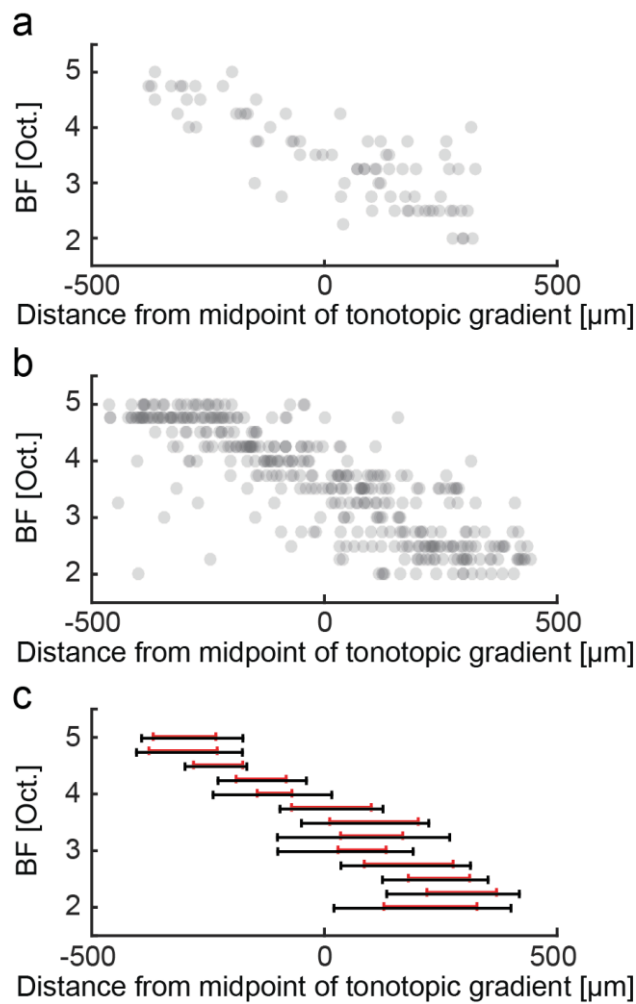
Figure 4.29: Variability of BF responses along the tonotopic axis

a. For the example recording shown in figure 4.23, the BFs of all frequency-tuned neurons are plotted according to their distance from the midpoint of the tonotopic axis (grey symbols). BFs ranging from 2-5 octaves are shown.

b. Together with the example data shown in panel a, a total of n = 5 independent experiments are overlaid.

c. Graph showing the distributions of single-cell BFs according to their distance from the midpoint of the tonotopic axis. Red lines show the IQR 50%, black lines show 2 x standard deviations.
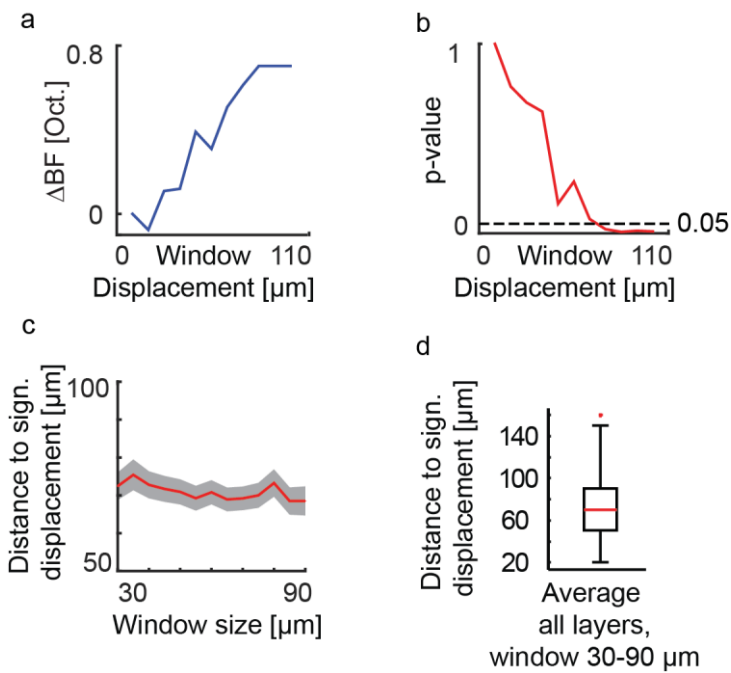
Figure 4.30: Analysis parameters to determine the distance along the tonotopic gradient for a significant BF difference

a. The difference of median BF (ΔBF) between the two analysis windows plotted according to their displacement along the tonotopic axis. Data used here is based on the example region shown in figure 4.28.

b. Same data as shown in panel a. The significance (p-value) of the difference between the average BF values in the two analysis windows is plotted against the distance between the two analysis windows. p < 0.05 = black dotted line.

c. Relationship between analysis window size and the distance along the tonotopic axis necessary to reach a significant displacement. Red line = average, grey shade = s.e.m. Window sizes ranging from 30 to 90 μm showed no statistically significant difference (Kruskal-Wallis test, χ^2 = 2.4, p = 0.999).

d. For analysis window sizes with 30-90 μm widths, the average distance to reach a significant BF difference in all layers was calculated.

5. Discussion

In conclusion, we developed an approach based on two-photon Ca^{2+} imaging to image neuronal activity with single-cell resolution in all layers of the cortex, and used the new technique in combination with autofluorescence imaging and 'conventional' two-photon imaging methods to analyze the spatial arrangement of best frequency (BF) responses in mouse primary auditory cortex with single-cell resolution.

The technical approach we used to map neuronal responses in all layers was based on a modified multi-cell bolus loading protocol (Stosiek *et al.*, 2003) using synthetic Ca^{2+}-indicators. With the red-shifted Ca^{2+} indicator Cal-590, we were able for the first time to image action potential-related somatic Ca^{2+} transients 900 μm below the cortical surface. Besides the advantage for imaging in deeper layers of the cortex, another potential application for Cal-590 is to image neuronal activity with two spectrally separate Ca^{2+} indicators at the same time. For example, Cal-590 can be imaged simultaneously with Cal-520 or OGB-1. A possible use of combined recordings is the parallel analysis of Ca^{2+} transients in two separate neuronal compartments (e.g. dendrites of one neuron vs. surrounding cell bodies, pre- vs. postsynaptic site etc.) or different cells in the same sample to study their functional relationship. Alternatively, Cal-590 AM can be used for a sequential experimental configuration to screen neuronal populations. In this kind of experiment, a population of neurons is labeled with the 'red' Cal-590, and a target neuron showing a specific kind of activity (such as a clear response to sensory stimulation) is identified. Next, this pre-selected neuron is selectively labeled with a spectrally separate 'green' Ca^{2+} indicator like Cal-520 or OGB-1 by single-cell electroporation or through a patch-clamp pipette in the whole-cell configuration. Two-photon imaging recordings from such a selectively 'green'-labeled neuron have the added advantage of reduced background-

contamination, as all other neurons in the sample are only labeled in 'red' and do not spoil the signal of the 'green' fluorescence channel. This experimental configuration could be especially advantageous for recordings which require subcellular resolution for the study of dendrites or dendritic spines in vivo (Chen *et al.*, 2011).

In recent years, genetically-encoded Ca^{2+} indicators have become increasingly powerful tools to analyze neuronal network function in vivo (Chen *et al.*, 2013). Their brightness and the possibility to record neuronal activity from the same cells across many different sessions makes them the Ca^{2+} indicator of choice for many imaging applications. However, for mapping a column-like structure in cortex, we used an approach based on multi-cell bolus loading of AM-type fluorescent dyes for two reasons: While genetically-encoded indicators allow for selective labeling of molecularly defined neuronal subgroups, the transfection efficiency with adenoviruses typically does not reach 100 % of the target cells. Other reports have indicated an inhomogeneous staining efficiency cross different cortical layers, with omission of layer 4 (Peron *et al.*, 2015). Thus, for our mapping effort, which aimed to include all cells in a given region, AM dyes are the more efficient probe. Furthermore, genetically-encoded indicators such as GCaMP6 are bright enough to allow for imaging in deeper cortical layers despite their excitation wavelengths around 920 nm, which makes them an ideal choice for the selective analysis of neuronal activity in specific subgroups in, for example, layer 5 (Mittmann *et al.*, 2011). However, if neurons in multiple densely labeled layers of the cortex have to be imaged in the same animal, a bright indicator such as GCaMP6 expressed throughout the entire depth of the cortex has the disadvantage of strong out-of-focus fluorescence lowering the signal quality in deeper imaging regions (Helmchen & Denk, 2005). Thus, very bright indicators are highly suitable for deep-imaging experiments with sparse labeling conditions, but reach a depth-limit in densely labeled tissue above layer 6 (Kondo *et al.*, 2016). We avoided the problem of out-focus fluorescence from overlying brain tissue by sequentially labeling each cortical layer, and by staining and imaging the deepest cortical layer first. This approach allowed us for the first time to

measure neuronal activity in all cortical layers at the same cortical location. The method is could be extended for use in species with larger brains in combination with, for example, three-photon imaging (Ouzounov *et al.*, 2017).

How does the functional micro-architecture revealed by our recordings relate to previous work in other cortical areas? In the visual cortex, the functional organization of the upper cortical layers was analyzed with single-cell resolution in vivo (Ohki *et al.*, 2005; Ohki *et al.*, 2006). Based on the work, three distinct types of cortical organization were described for direction-selectivity of individual neurons responding to drifting grating stimulation (Ohki *et al.*, 2005). First, layer 2/3 of rat visual cortex showed a random representation of directions without any discernable pattern. Secondly, layer 2/3 of cat visual cortex cells showed highly uniform areas, in which cells selective for specific directions are grouped together or form smooth direction gradients. Thirdly, the homogeneous areas observed in cats have sharp edges that culminate in so-called pinwheels (Ohki *et al.*, 2006), which are characterized by abrupt changed of directions along a very short micrometer-scale. Two-photon imaging studies in the somatosensory barrel cortex in rodents (Varga *et al.*, 2011; Jia *et al.*, 2014) described a strict whisker-specific functional organization in cortical layer 4 (Jia *et al.*, 2014), which becomes less specific in layer 2/3 by additional inputs from surround whiskers (Varga *et al.*, 2011). Thus, the narrow-band variability of BF responses arranged along the tonotopic gradient in all layers of the primary auditory cortex represents a functional organization pattern distinct from previous observations.

The concept of columns in auditory cortex has been suggested for decades (Oonishi & Katsuki, 1965; Abeles & Goldstein, 1970; Merzenich et al., 1975). However, observations of a cellular-scale local BF heterogeneity (Bandyopadhyay et al., 2010; Rothschild et al., 2010; Winkowski & Kanold, 2013) seemed to be at odds with such a columnar organization. How can functional columns be observed with locally heterogeneous cellular responses? Our findings address this apparent discrepancy: First, we confirmed locally heterogeneous BF responses in the upper cortical

layers, and found a similar degree of heterogeneity also in layers 4, 5 and 6. Interestingly, the similar degree of heterogeneity of layers 2/3 and 4 does not fit reports of a more homogeneous BF response in layer 4 (Winkowski & Kanold, 2013), but could possibly reflect effects of the isoflurane anesthesia used in the previous study. Secondly, we found local BF gradients at much shorter distances than reported before (Bandyopadhyay et al., 2010; Rothschild et al., 2010; Winkowski & Kanold, 2013). Together, the local BF heterogeneity and BF gradients explain why no significant BF difference can be observed along short distances (<100 μm) of the tonotopic axis. Thus, measurements with multi-electrode recordings spaced 80-90 μm apart might historically have been interpreted as discrete frequency columns. Our results show that a more accurate description of the microarchitecture is not one of discrete frequency-columns, but of 'sliding'-columns, which have a defined width around 70-80 μm at any given location along the tonotopic gradient. Future studies will have to determine how the lack of sharp boundaries between functional columns along the tonotopic axis may reflect the fact that in all cortical layers, individual neurons have hundreds of microns wide dendritic trees that may integrate stimuli with an extended range of frequencies (Chen *et al.*, 2011). In line with such a potential organization, it was recently reported that thalamocortical axonal inputs to the primary auditory cortex show a local heterogeneity with a similar variability in cortical layers 1 and 3b/4 (Vasquez-Lopez et al., 2017).

Furthermore, it remains to be elucidated whether the functional cellular-scale topography we found in mice is present in other species. However, it is worth noting that the macro-scale tonotopic organization of the primary auditory cortex is preserved across a wide range of species. For example, tonotopy has been shown in rodents (Stiebler *et al.*, 1997; Hackett *et al.*, 2011; Guo *et al.*, 2012), carnivores (Merzenich *et al.*, 1975; Bizley *et al.*, 2005), and non-human primates (Merzenich & Brugge, 1973). Therefore, the micro-architecture of functional columns described here could reflect a basic functional pattern for the representation of sensory stimuli in the mammalian brain.

In summary, we have developed a new approach to image column-like structures extending through the entire depth of the cortex to about 900 µm below the brain surface. With this technique, we demonstrated that the brain surface tonotopy of the primary auditory cortex is highly preserved throughout all layers at the single-neuron level despite heterogeneous frequency-dependent tone responses of neighboring neurons. Additionally, the analysis of the cellular response maps revealed a smooth organizational pattern of the primary auditory cortex. Thus, our findings bridge the gap between the brain surface sensory map and the single-neuron functional topography in all layers of the primary auditory cortex.

6. References

Abeles M & Goldstein MH, Jr. (1970). Functional architecture in cat primary auditory cortex: columnar organization and organization according to depth. *J Neurophysiol* **33,** 172-187.

Andersen RA, Snyder RL & Merzenich MM. (1980). The topographic organization of corticocollicular projections from physiologically identified loci in the AI, AII, and anterior auditory cortical fields of the cat. *J Comp Neurol* **191,** 479-494.

Anderson LA, Christianson GB & Linden JF. (2009). Mouse auditory cortex differs from visual and somatosensory cortices in the laminar distribution of cytochrome oxidase and acetylcholinesterase. *Brain Res* **1252,** 130-142.

Bandyopadhyay S, Shamma SA & Kanold PO. (2010). Dichotomy of functional organization in the mouse auditory cortex. *Nat Neurosci* **13,** 361-368.

Barkat TR, Polley DB & Hensch TK. (2011). A critical period for auditory thalamocortical connectivity. *Nat Neurosci* **14,** 1189-1194.

Barnstedt O, Keating P, Weissenberger Y, King AJ & Dahmen JC. (2015). Functional Microarchitecture of the Mouse Dorsal Inferior Colliculus Revealed through In Vivo Two-Photon Calcium Imaging. *J Neurosci* **35,** 10927-10939.

References

Berridge MJ, Lipp P & Bootman MD. (2000). The versatility and universality of calcium signalling. *Nat Rev Mol Cell Biol* **1,** 11-21.

Birkner A, Tischbirek CH & Konnerth A. (2017). Improved deep two-photon calcium imaging in vivo. *Cell Calcium* **64,** 29-35.

Bizley JK, Nodal FR, Nelken I & King AJ. (2005). Functional organization of ferret auditory cortex. *Cereb Cortex* **15,** 1637-1653.

Blasdel GG & Salama G. (1986). Voltage-sensitive dyes reveal a modular organization in monkey striate cortex. *Nature* **321,** 579-585.

Bonhoeffer T & Grinvald A. (1991). Iso-Orientation Domains in Cat Visual-Cortex Are Arranged in Pinwheel-Like Patterns. *Nature* **353,** 429-431.

Brodmann K. (1909). *Vergleichende Lokalisationslehre der Grosshirnrinde in ihren Prinzipien dargestellt auf Grund des Zellenbaues von Dr. K. Brodmann*. J.A. Barth.

Brustein E, Marandi N, Kovalchuk Y, Drapeau P & Konnerth A. (2003). "In vivo" monitoring of neuronal network activity in zebrafish by two-photon Ca(2+) imaging. *Pflugers Arch* **446,** 766-773.

Busche MA, Chen X, Henning HA, Reichwald J, Staufenbiel M, Sakmann B & Konnerth A. (2012). Critical role of soluble amyloid-beta for early hippocampal hyperactivity in a mouse model of Alzheimer's disease. *Proc Natl Acad Sci U S A* **109,** 8740-8745.

Chen TW, Wardill TJ, Sun Y, Pulver SR, Renninger SL, Baohan A, Schreiter ER, Kerr RA, Orger MB, Jayaraman V, Looger LL, Svoboda K & Kim

DS. (2013). Ultrasensitive fluorescent proteins for imaging neuronal activity. *Nature* **499,** 295-300.

Chen X, Leischner U, Rochefort NL, Nelken I & Konnerth A. (2011). Functional mapping of single spines in cortical neurons in vivo. *Nature* **475,** 501-505.

Christianson GB, Sahani M & Linden JF. (2011). Depth-dependent temporal response properties in core auditory cortex. *J Neurosci* **31,** 12837-12848.

Fierro L & Llano I. (1996). High endogenous calcium buffering in Purkinje cells from rat cerebellar slices. *The Journal of physiology* **496 (Pt 3),** 617-625.

Glasser MF, Coalson TS, Robinson EC, Hacker CD, Harwell J, Yacoub E, Ugurbil K, Andersson J, Beckmann CF, Jenkinson M, Smith SM & Van Essen DC. (2016). A multi-modal parcellation of human cerebral cortex. *Nature* **536,** 171-178.

Grienberger C & Konnerth A. (2012). Imaging calcium in neurons. *Neuron* **73,** 862-885.

Guo W, Chambers AR, Darrow KN, Hancock KE, Shinn-Cunningham BG & Polley DB. (2012). Robustness of cortical topography across fields, laminae, anesthetic states, and neurophysiological signal types. *J Neurosci* **32,** 9159-9172.

Hackett TA, Barkat TR, O'Brien BM, Hensch TK & Polley DB. (2011). Linking topography to tonotopy in the mouse auditory thalamocortical circuit. *J Neurosci* **31,** 2983-2995.

Hagihara KM, Murakami T, Yoshida T, Tagawa Y & Ohki K. (2015). Neuronal activity is not required for the initial formation and maturation of visual selectivity. *Nat Neurosci* **18,** 1780-1788.

Helmchen F & Denk W. (2005). Deep tissue two-photon microscopy. *Nat Methods* **2,** 932-940.

Hubel DH & Wiesel TN. (1968). Receptive Fields and Functional Architecture of Monkey Striate Cortex. *J Physiol-London* **195,** 215-&.

Inoue M, Takeuchi A, Horigane S, Ohkura M, Gengyo-Ando K, Fujii H, Kamijo S, Takemoto-Kimura S, Kano M, Nakai J, Kitamura K & Bito H. (2015). Rational design of a high-affinity, fast, red calcium indicator R-CaMP2. *Nat Methods* **12,** 64-70.

Issa JB, Haeffele BD, Agarwal A, Bergles DE, Young ED & Yue DT. (2014). Multiscale optical Ca2+ imaging of tonal organization in mouse auditory cortex. *Neuron* **83,** 944-959.

Ji N. (2017). Adaptive optical fluorescence microscopy. *Nature Methods* **14,** 374-380.

Ji N, Sato TR & Betzig E. (2012). Characterization and adaptive optical correction of aberrations during in vivo imaging in the mouse cortex. *Proc Natl Acad Sci U S A* **109,** 22-27.

Jia H, Varga Z, Sakmann B & Konnerth A. (2014). Linear integration of spine Ca2+ signals in layer 4 cortical neurons in vivo. *Proc Natl Acad Sci U S A* **111,** 9277-9282.

Kalatsky VA, Polley DB, Merzenich MM, Schreiner CE & Stryker MP. (2005). Fine functional organization of auditory cortex revealed by Fourier optical imaging. *Proc Natl Acad Sci U S A* **102,** 13325-13330.

Kanold PO, Nelken I & Polley DB. (2014). Local versus global scales of organization in auditory cortex. *Trends Neurosci* **37,** 502-510.

Kato HK, Gillet SN & Isaacson JS. (2015). Flexible Sensory Representations in Auditory Cortex Driven by Behavioral Relevance. *Neuron* **88,** 1027-1039.

Kerlin AM, Andermann ML, Berezovskii VK & Reid RC. (2010). Broadly tuned response properties of diverse inhibitory neuron subtypes in mouse visual cortex. *Neuron* **67,** 858-871.

Kitamura K, Judkewitz B, Kano M, Denk W & Hausser M. (2008). Targeted patch-clamp recordings and single-cell electroporation of unlabeled neurons in vivo. *Nat Methods* **5,** 61-67.

Kobat D, Durst ME, Nishimura N, Wong AW, Schaffer CB & Xu C. (2009). Deep tissue multiphoton microscopy using longer wavelength excitation. *Optics express* **17,** 13354-13364.

Komiyama T, Sato TR, O'Connor DH, Zhang YX, Huber D, Hooks BM, Gabitto M & Svoboda K. (2010). Learning-related fine-scale specificity imaged in motor cortex circuits of behaving mice. *Nature* **464,** 1182-1186.

Kondo S, Yoshida T & Ohki K. (2016). Mixed functional microarchitectures for orientation selectivity in the mouse primary visual cortex. *Nat Commun* **7,** 13210.

Larionow W. (1899). Ueber die musikalischen Centren des Gehirns. *Archiv für die gesamte Physiologie des Menschen und der Tiere* **76,** 608-625.

Lee SH, Rosenmund C, Schwaller B & Neher E. (2000). Differences in Ca2+ buffering properties between excitatory and inhibitory hippocampal neurons from the rat. *The Journal of physiology* **525 Pt 2,** 405-418.

Li J, Zhang J, Wang M, Pan J, Chen X & Liao X. (2017). Functional imaging of neuronal activity of auditory cortex by using Cal-520 in anesthetized and awake mice. *Biomed Opt Express* **8,** 2599-2610.

Li N, Chen TW, Guo ZV, Gerfen CR & Svoboda K. (2015). A motor cortex circuit for motor planning and movement. *Nature* **519,** 51-56.

Linden JF, Liu RC, Sahani M, Schreiner CE & Merzenich MM. (2003). Spectrotemporal structure of receptive fields in areas AI and AAF of mouse auditory cortex. *J Neurophysiol* **90,** 2660-2675.

Longair MH, Baker DA & Armstrong JD. (2011). Simple Neurite Tracer: open source software for reconstruction, visualization and analysis of neuronal processes. *Bioinformatics* **27,** 2453-2454.

Merzenich MM & Brugge JF. (1973). Representation of the cochlear partition of the superior temporal plane of the macaque monkey. *Brain Res* **50,** 275-296.

References

Merzenich MM, Knight PL & Roth GL. (1975). Representation of cochlea within primary auditory cortex in the cat. *J Neurophysiol* **38,** 231-249.

Mittmann W, Wallace DJ, Czubayko U, Herb JT, Schaefer AT, Looger LL, Denk W & Kerr JN. (2011). Two-photon calcium imaging of evoked activity from L5 somatosensory neurons in vivo. *Nat Neurosci* **14,** 1089-1093.

Mountcastle V, Berman A & Davies P. (1955). Topographic organization and modality representation in first somatic area of cat's cerebral cortex by method of single unit analysis. *American Journal of Physiology*.

Mutze J, Iyer V, Macklin JJ, Colonell J, Karsh B, Petrasek Z, Schwille P, Looger LL, Lavis LD & Harris TD. (2012). Excitation spectra and brightness optimization of two-photon excited probes. *Biophys J* **102,** 934-944.

Nauhaus I, Nielsen KJ, Disney AA & Callaway EM. (2012). Orthogonal micro-organization of orientation and spatial frequency in primate primary visual cortex. *Nat Neurosci* **15,** 1683-1690.

Nichols RA & Mollard P. (1996). Direct observation of serotonin 5-HT3 receptor-induced increases in calcium levels in individual brain nerve terminals. *J Neurochem* **67,** 581-592.

Oheim M, van 't Hoff M, Feltz A, Zamaleeva A, Mallet JM & Collot M. (2014). New red-fluorescent calcium indicators for optogenetics, photoactivation and multi-color imaging. *Biochimica et biophysica acta* **1843,** 2284-2306.

Ohki K, Chung S, Ch'ng YH, Kara P & Reid RC. (2005). Functional imaging with cellular resolution reveals precise micro-architecture in visual cortex. *Nature* **433,** 597-603.

Ohki K, Chung S, Kara P, Hubener M, Bonhoeffer T & Reid RC. (2006). Highly ordered arrangement of single neurons in orientation pinwheels. *Nature* **442,** 925-928.

Oonishi S & Katsuki Y. (1965). Functional organization and integrative mechanism on the auditory cortex of the cat. *The Japanese Journal of Physiology* **15,** 342-365.

Ouzounov DG, Horton N, Wang T, Feng D, Nishimura N & Xu C. (2014). In Vivo Three-photon Calcium Imaging of Brain Activity from Layer 6 Neurons in Mouse Brain. In *CLEO: 2014 Postdeadline Paper Digest*, pp. STh5C.2. Optical Society of America, San Jose, California.

Ouzounov DG, Wang T, Wang M, Feng DD, Horton NG, Cruz-Hernandez JC, Cheng YT, Reimer J, Tolias AS, Nishimura N & Xu C. (2017). In vivo three-photon imaging of activity of GCaMP6-labeled neurons deep in intact mouse brain. *Nat Methods* **14,** 388-390.

Perillo EP, McCracken JE, Fernee DC, Goldak JR, Medina FA, Miller DR, Yeh HC & Dunn AK. (2016). Deep in vivo two-photon microscopy with a low cost custom built mode-locked 1060 nm fiber laser. *Biomed Opt Express* **7,** 324-334.

Peron SP, Freeman J, Iyer V, Guo C & Svoboda K. (2015). A Cellular Resolution Map of Barrel Cortex Activity during Tactile Behavior. *Neuron* **86,** 783-799.

Petersen CC. (2007). The functional organization of the barrel cortex. *Neuron* **56,** 339-355.

Pilz GA, Carta S, Stauble A, Ayaz A, Jessberger S & Helmchen F. (2016). Functional Imaging of Dentate Granule Cells in the Adult Mouse Hippocampus. *J Neurosci* **36,** 7407-7414.

Rathouz MM & Berg DK. (1994). Synaptic-type acetylcholine receptors raise intracellular calcium levels in neurons by two mechanisms. *J Neurosci* **14,** 6935-6945.

Rothschild G, Nelken I & Mizrahi A. (2010). Functional organization and population dynamics in the mouse primary auditory cortex. *Nat Neurosci* **13,** 353-360.

Sadakane O, Masamizu Y, Watakabe A, Terada S, Ohtsuka M, Takaji M, Mizukami H, Ozawa K, Kawasaki H, Matsuzaki M & Yamamori T. (2015). Long-Term Two-Photon Calcium Imaging of Neuronal Populations with Subcellular Resolution in Adult Non-human Primates. *Cell Rep* **13,** 1989-1999.

Sawinski J, Wallace DJ, Greenberg DS, Grossmann S, Denk W & Kerr JN. (2009). Visually evoked activity in cortical cells imaged in freely moving animals. *Proc Natl Acad Sci U S A* **106,** 19557-19562.

Schneggenburger R, Zhou Z, Konnerth A & Neher E. (1993). Fractional contribution of calcium to the cation current through glutamate receptor channels. *Neuron* **11,** 133-143.

References

Schreiner CE & Winer JA. (2007). Auditory cortex mapmaking: principles, projections, and plasticity. *Neuron* **56,** 356-365.

Seelig JD, Chiappe ME, Lott GK, Dutta A, Osborne JE, Reiser MB & Jayaraman V. (2010). Two-photon calcium imaging from head-fixed Drosophila during optomotor walking behavior. *Nat Methods* **7,** 535-540.

Smith AM, Mancini MC & Nie S. (2009). Bioimaging: second window for in vivo imaging. *Nature nanotechnology* **4,** 710-711.

Sordillo LA, Pu Y, Pratavieira S, Budansky Y & Alfano RR. (2014). Deep optical imaging of tissue using the second and third near-infrared spectral windows. *J Biomed Opt* **19,** 056004.

Stiebler I, Neulist R, Fichtel I & Ehret G. (1997). The auditory cortex of the house mouse: left-right differences, tonotopic organization and quantitative analysis of frequency representation. *J Comp Physiol A* **181,** 559-571.

Stirman JN, Smith IT, Kudenov MW & Smith SL. (2016). Wide field-of-view, multi-region, two-photon imaging of neuronal activity in the mammalian brain. *Nature Biotechnology* **34,** 857-+.

Stosiek C, Garaschuk O, Holthoff K & Konnerth A. (2003). In vivo two-photon calcium imaging of neuronal networks. *Proc Natl Acad Sci U S A* **100,** 7319-7324.

Tada M, Takeuchi A, Hashizume M, Kitamura K & Kano M. (2014). A highly sensitive fluorescent indicator dye for calcium imaging of neural activity in vitro and in vivo. *Eur J Neurosci* **39,** 1720-1728.

Takahashi K, Hishida R, Kubota Y, Kudoh M, Takahashi S & Shibuki K. (2006). Transcranial fluorescence imaging of auditory cortical plasticity regulated by acoustic environments in mice. *Eur J Neurosci* **23,** 1365-1376.

Tischbirek C, Birkner A, Jia H, Sakmann B & Konnerth A. (2015). Deep two-photon brain imaging with a red-shifted fluorometric Ca2+ indicator. *Proc Natl Acad Sci U S A* **112,** 11377-11382.

Tischbirek CH, Birkner A & Konnerth A. (2017). In vivo deep two-photon imaging of neural circuits with the fluorescent Ca(2+) indicator Cal-590. *The Journal of physiology* **595,** 3097-3105.

Tsien RY. (1981). A non-disruptive technique for loading calcium buffers and indicators into cells. *Nature* **290,** 527-528.

Tsukano H, Horie M, Ohga S, Takahashi K, Kubota Y, Hishida R, Takebayashi H & Shibuki K. (2017). Reconsidering Tonotopic Maps in the Auditory Cortex and Lemniscal Auditory Thalamus in Mice. *Front Neural Circuits* **11,** 14.

Van Essen DC & Dierker DL. (2007). Surface-based and probabilistic atlases of primate cerebral cortex. *Neuron* **56,** 209-225.

Varga Z, Jia H, Sakmann B & Konnerth A. (2011). Dendritic coding of multiple sensory inputs in single cortical neurons in vivo. *Proc Natl Acad Sci U S A* **108,** 15420-15425.

References

Vasquez-Lopez SA, Weissenberger Y, Lohse M, Keating P, King AJ & Dahmen JC. (2017). Thalamic input to auditory cortex is locally heterogeneous but globally tonotopic. *Elife* **6**.

Vazquez G, Wedel BJ, Aziz O, Trebak M & Putney JW, Jr. (2004). The mammalian TRPC cation channels. *Biochimica et biophysica acta* **1742,** 21-36.

Wandell BA, Dumoulin SO & Brewer AA. (2007). Visual field maps in human cortex. *Neuron* **56,** 366-383.

Wang K, Sun W, Richie CT, Harvey BK, Betzig E & Ji N. (2015). Direct wavefront sensing for high-resolution in vivo imaging in scattering tissue. *Nat Commun* **6,** 7276.

Webster DB & Fay RR. (2013). *The mammalian auditory pathway: neuroanatomy*, vol. 1. Springer Science & Business Media.

Winkowski DE & Kanold PO. (2013). Laminar transformation of frequency organization in auditory cortex. *J Neurosci* **33,** 1498-1508.

Xu C & Webb WW. (1996). Measurement of two-photon excitation cross sections of molecular fluorophores with data from 690 to 1050 nm. *J Opt Soc Am B* **13,** 481-491.

Xu C & Wise FW. (2013). Recent advances in fibre lasers for nonlinear microscopy. *Nat Photon* **7,** 875-882.

Zhao Q, Guo H, Yi G, Liao J & Diwu Z. (2015). A Novel Red Fluorescence Calcium Indicator for Functional Analysis of GPCRs and Calcium Channel Targets. *Biophysical Journal* **108,** 109a-110a.

7.   Acknowledgements